Proposal for an experiment at the 50-GeV PS

Measurement of the differential cross section and spin observables of the Λp scattering with a polarized Λ beam

K. Miwa(spokesperson), S. H. Hayakawa, Y. Ishikawa, K. Itabashi, K. Kamada, T. Kitaoka, T. Morino, S. Nagao, S. N. Nakamura, F. Oura, T. Sakao, H. Tamura, H. Umetsu, S. Wada
Tohoku University, Japan

M. Fujita, Y. Ichikawa, T. O. Yamamoto
Japan Atomic Energy Agency (JAEA), Japan

R. Honda, M. Ieiri, T. Takahashi, M. Ukai
High Energy Accelerator Research Organization (KEK), Japan

T. Nanamura
Kyoto University, Japan

K. Shirotori
Research Center for Nuclear Physics (RCNP), Osaka University, Japan

P. Evtoukhovitch
Joint Institute for Nuclear Research (JINR), Russia

Z. Tsamalaidze
Joint Institute for Nuclear Research (JINR), Russia
Georgian Technical University (GTU), Tbilisi, Georgia

Abstract

We request 34-days beam time including 29-days production run and 5-days commissioning and calibration runs as first stage to measure the differential cross section and the Analyzing power of the Λp scattering by accumulating 50M momentum-tagged Λ beam. As second stage, we request additional 34-days beam time including the production and commissioning/calibration runs with the same ratio to measure the depolarization and to improve the accuracy of measurements of the differential cross section and Analyzing power. Here, we assume that spill structure is 5.2 s cycle with a beam duration of 2 s and the π^- beam intensity is 30 M/spill. As the final goal, we will measure differential cross sections of the Λp elastic scattering with better than 10% statistical error with an angular step of $d\cos\theta$=0.1 for each 50 MeV/c Λ beam momentum step from 0.4 to 0.8 GeV/c. Analyzing power and depolarization are measured with a 10% level statistical error with an angular step of $d\cos\theta$=0.2 for each 100 MeV/c Λ beam momentum step from 0.4 to 0.8 GeV/c. The experimental setup is almost the same with that in the E40 experiment (Σp scattering) which consists of two detector components. The first component is the K1.1 beam-line and SKS spectrometers to identify Λ particles produced inside a liquid hydrogen target of 30 cm long. The second component is the recoil proton detector system (CATCH) to identify the Λp scattering event kinematically by detecting the recoil proton and the scattered Λ. From the analysis of the by-product data in E40, Λp scattering events are already identified clearly with this method.

This is the first experimental attempt to measure not only the differential cross section but also the spin observables such as Analyzing power and depolarization by using almost 100% polarized Λ beam produced by the $\pi^- p \to K^0\Lambda$ reaction at p_{π^-}=1.05 GeV/c. Although there exist several Λp scattering data in the "hydrogen bubble chamber" era, such data are mostly limited in the low Λ momentum region around 0.3 GeV/c. In addition, there is no differential observables such as differential cross section. Due to such limited experimental information, the theoretical models of baryon-baryon (BB) interactions show quite different predictions for the P-wave and higher-wave momentum regions even for the ΛN interaction which has been intensively studied from Λ hypernuclei. In such momentum region, the strength of the spin-dependent interaction such as LS force becomes sizable. In order to impose a strong constraint on the theoretical models for getting the realistic description of BB two-body interaction, a lot of scattering observables including the spin observables are essential. For example, in chiral effective field theory, the low energy constant (LEC), which should be fixed from experimental data, for P wave will be determined well from these experimental data.

Currently, it is really important to establish "realistic" BB interaction models with both theoretical and experimental efforts to solve so called "hyperon puzzle" in neutron stars. In order to support massive neutron star with two-solar mass, repulsive force due to multi-baryon force including ΛNN interaction is expected to play a key role. Such many-body effect is expected to appear in the heavy Λ hypernuclei as the mass difference in the ground state. A new project just launched to explore the ΛNN three-body interaction by measuring the Λ hypernuclear binding energy ultra-pricisely via the (π^+, K^+) spectroscopy in the extended hadron experimental facility by utilizing a high-intensity high-resolution (HIHR) beam line. Our hyperon-proton scattering experiment is also the base ground to reinforce

such strategy by establishing the realistic BB interaction in collaboration with theoretical groups of modern BB interaction models.

Contents

Chapter 1

Physics motivation

1.1 Background of YN interaction and YN scattering experiment

Nucleus is a many-body system of nucleons which are bound by a nuclear force. The nuclear force is crucially important interaction which determines the structures from nuclei up to compact stars. The nuclear force shows the attractive nature in the middle and long ranges and the averaged attractive force binds the nuclei. In order to make the nuclei and compact stars be a stable bound state, the balance between the attractive force in the middle-long range and repulsive force in the short range is very important, because the repulsive force in the short range prevents nuclei and compact stars from collapsing due to its attractive force. The nuclear force is a strong interaction between the color-less nucleon and can be described theoretically by not taking into account the role of quarks. For example, boson exchange models try to explain the nuclear force by considering the possible meson exchange including pseudo scalar, vector, scalar mesons and its pair or multi-meson exchange diagrams. Experimentally, the nuclear force has been intensively studied by plenty of proton-proton and neutron-proton scattering experiments. Very precise scattering data such as differential cross section and spin observables exist and these data were essential to construct so-called "realistic models" [1, 2, 3] for nuclear force which reproduce these experimental observables with a reduced $\chi^2 \sim 1$. Such modern interaction models are used to understand the structure of the nuclei and three-body nuclear force.

In order to understand the role of quarks in the nuclear force, we should extend the nuclear force to the baryon-baryon (BB) interaction including hyperon-nucleon (YN) and hyperon-hyperon (YY) interactions, because new interaction-multiplets are expected to show very different features in the short range region where two baryons overlap with each other. The quark cluster model predicts the quite repulsive core in the 10 and 8_s multiplets due to the Pauli effect in quark level and the attractive core in the flavor singlet channel due to the color-magnetic interaction [4, 5]. These predictions are now reproduced by lattice QCD simulations which become a powerful theoretical tool to derive the YN and YY potentials from the first principle in QCD [6, 7, 8]. The BB interaction is an essential test to describe the meson exchange picture with a uniform treatment assuming the SU(3) flavor symmetry [9, 10, 11]. In order to test these theoretical models of two-body BB interaction, important experimental inputs are the binding energy of few-body bound system including hyperon such as hypertriton and two-body scattering data between hyperon and proton. As we

mentioned, the pp and np scattering data played an essential role to establish the realistic nuclear force models. On the other hand, the hyperon-proton scattering experiment was quite difficult experimentally due to the low intensity of the hyperon beam and its short lifetime. 36 cross section data of the Λp and Σp scatterings [12, 13, 14, 15, 16, 17, 18, 19, 20] were actually indispensable to construct the present BB interaction models. However the quality and quantity of these data are insufficient to impose a strict constraint on the theoretical models. Therefore, historically, the BB interaction has been investigated from the hypernuclear structure because their binding energies and level structures reflect the YN interaction [21]. The effective two-body interaction potential in the hypernuclei was obtained by the G-matrix calculation using the bare two-body interaction [22]. Then, the calculated energy levels of the hypernulear system were compared with the hypernuclear data and the bare two-body interaction was updated so as to reproduce the experimental data. This theoretical and experimental strategy seems to work well at least for the many hypernucler phenomena. However, we know that a neutron star with two-solar mass [23] can not be supported by the present two-body YN interaction due to softening of the equation of state by the appearance of hyperons in the high density region in the neutron star. The many-body repulsive interactions such as YNN three-body force are expected to play an essential role in the such high-density region to support the massive neutron star with hyperon. Such many-body effect is expected to appear in the heavy Λ hypernuclei as the mass difference in the ground state. A new project to measure the Λ hypernuclear bounding energy with ultra precise resolution are just launching to explore the ΛNN three-body interaction by the (π^+, K^+) spectroscopy in the extended hadron experimental facility by utilizing a high-intensity high-resolution (HIHR) beamline [24]. In such a situation, it is crucially important to establish the realistic two-body YN interaction from the two-body system, that is, YN scattering data. That is because the current theoretical treatment to derive YN two-body interaction from the hypernuclear structure is already suffered from uncertainties from the many-body effect in the hypernuclei. Therefore, we have to really change the strategy for deriving the YN two-body interaction, that is, the realistic two-body YN interaction should be constructed based on the two-body scattering data.

Recently, we have realized a high-statistics Σp scattering in the J-PARC E40 experiment where $\sim$5,000 scattering events for both $\Sigma^- p$ and $\Sigma^+ p$ channels were identified [25, 26]. We have introduced a new experimental technique to overcome the experimental difficulty of a hyperon-proton scattering experiment. A liquid hydrogen target was used as both hyperon production and hyperon proton scattering targets to identify the hyperon production and the scattering events kinematically without any imaging data to identify the scattering topology. High intensity π beams were handled to accumulate Σ beams as much as possible and more than 100 times more Σ beams ($\sim$17 M Σ^- and $\sim$70 M Σ^+) than that in the past KEK experiment were accumulated. Figure 1.1 [26] shows the differential cross sections measured in E40 together with a past measurement (KEK-PS E289 data for 400 $< p$ (MeV/c) $<$ 700 [19]) and theoretical calculations. The statistical error of 10% level was achieved with a fine angular step of $d\cos\theta = 0.1$ by identifying the largest statistics of about 4,500 $\Sigma^- p$ elastic scattering events from 1.72×10^7 Σ^- particles. The differential cross sections show clear forward peaking structure and the forward and backward ratio is large particularly in the higher momentum regions. Although the experimental inputs of the two-body hyperon-proton scattering were quite limited up to now, the success of the $\Sigma^- p$ scattering is a remarkable step to provide accurate data to improve the BB interaction models and to establish the realistic BB interactions with both theoretical and experimental

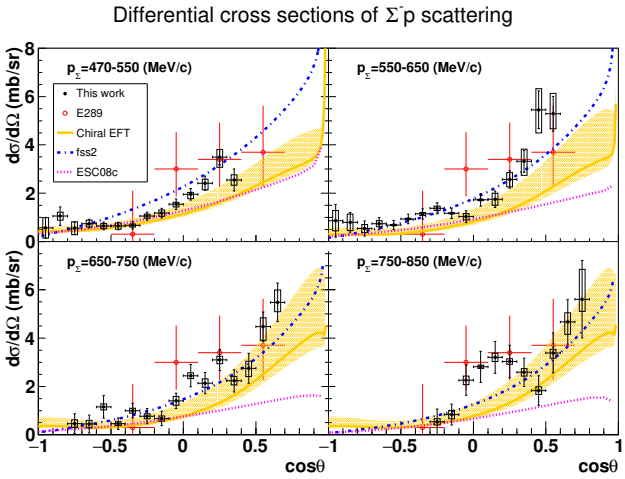

Figure 1.1: Differential cross sections obtained in the present experiment (black points) [26] . The error bars and boxes show statistical and systematic uncertainties, respectively. Red points are averaged differential cross section of $400 < p$ (MeV/c) < 700 taken in KEK-PS E289 (the same points are plotted in all of the four momentum regions). The dotted (magenta), dot-dashed (blue) and solid (yellow) lines represent the calculated cross sections by the Nijmegen ESC08c model based on boson-exchange picture, the fss2 model including QCM and the extended χEFT model, respectively.

efforts. We apply the same experimental method to the Λp scattering experiment to derive the differential cross section and spin observables with good accuracy. By synthesizing all the experimental information (ΣN channel in E40 and ΛN channel in the proposed experiment), better understanding of the BB interactions will be achieved in near future.

1.2 Formalism of the spin-dependent YN interaction

In this proposed experiment, the important new aspect is to measure the spin observables with a polarized Λ beam. The hyperon-proton scattering is the scattering between two spin 1/2 particles and the spin observables are substantial tool for the study of the spin-dependent YN interaction.

The T matrix for the elastic scattering between particle a and b is represented in terms of spin-independent, spin-spin, symmetric LS (SLS), antisymmetric LS (ALS) and tensor components as

$$M = V_c + V_\sigma(\boldsymbol{s_a}\cdot\boldsymbol{s_b}) + V_{SLS}(\boldsymbol{s_a}+\boldsymbol{s_b})\cdot\boldsymbol{L} + V_{ALS}(\boldsymbol{s_a}-\boldsymbol{s_b})\cdot\boldsymbol{L} + V_T([\boldsymbol{s_a}\otimes\boldsymbol{s_b}]^{(2)}\cdot\boldsymbol{Y_2}(\hat{\boldsymbol{r}})) \quad (1.1)$$

where $\boldsymbol{L}$ is the a-b relative orbital angular momentum, $\boldsymbol{r}$ is the a-b relative coordinate and V's are form-factor functions for the spin-independent central interaction V_c, the spin-spin interaction V_σ, the SLS interaction V_{SLS}, the ALS interaction V_{ALS}, and the tensor interaction V_T [27]. In order to describe the scattering observables, new scalar amplitudes, vector amplitudes and tensor amplitudes are defined as follows,

$$U_\alpha \equiv < \boldsymbol{k}_f|V_c|\boldsymbol{k}_i >, U_\beta \equiv < \boldsymbol{k}_f|V_\sigma|\boldsymbol{k}_i > \quad (1.2)$$

for the scalar amplitudes,

$$S_{ALS} \equiv < \boldsymbol{k}_f|V_{ALS}L_1|\boldsymbol{k}_i >, S_{ALS} \equiv < \boldsymbol{k}_f|V_{SLS}L_1|\boldsymbol{k}_i > \quad (1.3)$$

for the vector amplitudes and

$$T_j = \frac{1}{2} < \boldsymbol{k}_f | V_T Y_{2j-1} | \boldsymbol{k}_i > \tag{1.4}$$

for the tensor amplitudes for $j = 1, 2, 3$. For later convenience, the following T_α and T_β are also used,

$$T_\alpha = \frac{1}{\sqrt{6}} T_1 + T_3, T_\beta = \frac{1}{\sqrt{6}} T_1 - T_3, \tag{1.5}$$

which give

$$T_2 = -\tan\theta (\frac{1}{2} T_\alpha + T_\beta). \tag{1.6}$$

The differential cross section is described by the sum of the all contributions as follows,

$$\left(\frac{d\sigma}{d\Omega}\right) = \frac{1}{4}\mathrm{Tr}(MM^\dagger) = |U_\alpha|^2 + \frac{3}{16}|U_\beta|^2 + \frac{1}{2}(|S_{SLS}|^2 + |S_{ALS}|^2) + \frac{1}{4}|T_1|^2 + \frac{1}{2}(|T_2|^2 + |T_3|^2). \tag{1.7}$$

Therefore, in order to determine the each component separately, a lot of spin observables are necessary. In the YN scattering case, the measurable spin observables are limited. However, such spin observables data are quite important to pin down the each spin-dependent component. The analyzing power $A_y(Y)$ for the polarized hyperon beam is described as,

$$A_y(Y) = -\frac{1}{\sqrt{2}\sigma(\theta)} \mathrm{Im} \left\{ (U_\alpha + \frac{1}{4} U_\beta)^* S_{SLS} + (U_\alpha - \frac{1}{4} U_\beta)^* S_{ALS} - \frac{1}{2} T_\alpha^* (-S_{ALS} + S_{SLS}) \right\}, \tag{1.8}$$

where $\sigma(\theta)$ represents the differential cross section. If we consider the component including the tensor amplitude (T_α) is the 2nd order value, the analyzing power is sensitive to the LS and ALS forces. In the NN interaction, ALS is not allowed for the isospin symmetry and ALS is the purely the new interaction appeared in the YN sector.

By measuring the change of the polarization of hyperon before and after the scattering, the depolarization can be measured. The depolarization is described as

$$\begin{aligned} D_y^y = \frac{1}{\sigma(\theta)} \mathrm{Re} \Bigg\{ & \frac{1}{2\sqrt{3}} \left(U_0 + \frac{1}{\sqrt{3}} U_1 \right)^* U_1 + \frac{1}{2} \left(U_0 - \frac{1}{\sqrt{3}} U_1 \right)^* \left(\frac{1}{\sqrt{6}} T_1 + T_3 \right) - S_1^* S_2 \\ & + \frac{1}{2}|S_3|^2 - \frac{1}{\sqrt{6}} T_1^* \left(\frac{1}{\sqrt{6}} T_1 - T_3 \right) - \frac{1}{2}|T_2|^2 \Bigg\}. \end{aligned} \tag{1.9}$$

Although the equation is complicated form of several amplitudes, D_y^y is expected to be rather sensitive to tensor force [28]. It is still difficult to determine each spin-dependent component separately from these limited observables. However, accumulation of these differential measurements can contribute to impose strong constraints on the present YN interaction models.

As for the type of the existing YN scattering observables, total cross section data exist even though the accuracy is not sufficient. Therefore theoretical calculations of all models become similar for the total cross section because the existing cross section data are used to fit parameters in the theoretical models as shown in next section. However, since there are almost no spin observable data except for the analyzing power measured in KEK [29], the theoretical prediction are quite different among the different theoretical frameworks. Therefore the spin observable measurement is quite important to test and improve the theoretical frameworks.

1.3 Theoretical studies for the Λp scattering

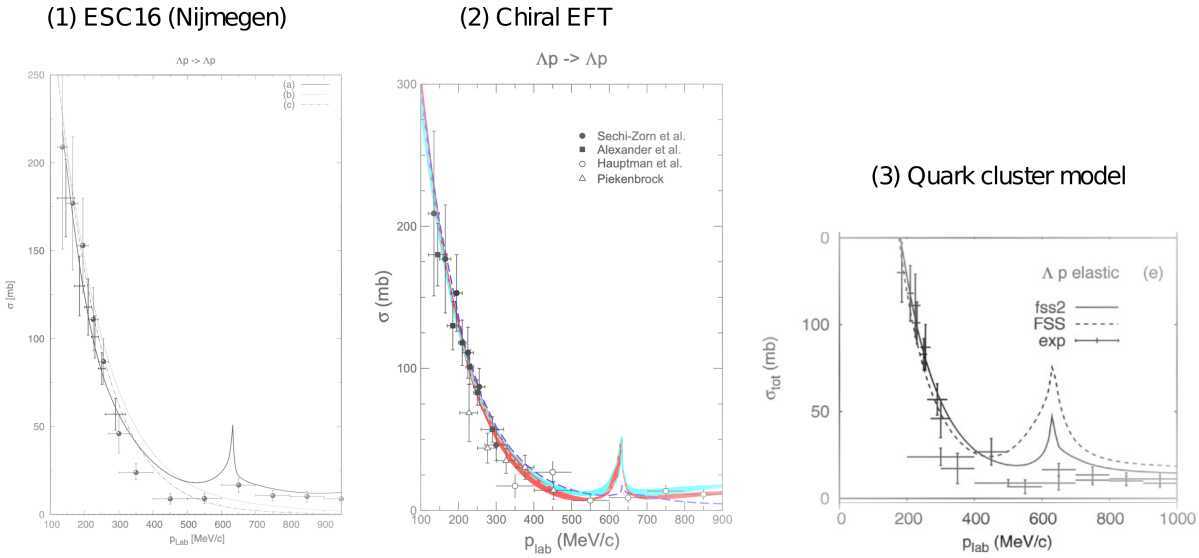

Figure 1.2: Total cross section of the Λp elastic scattering and theoretical calculation. (1)Calculation by ESC16 model [10]. The solid line (a) shows the calculation including the higher wave contribution, whereas dotted lines (b) and (c) are obtained by the effective range approximation with some scattering length and effective range. (2) Calculation by the chiral EFT model with contributions up to the next leading order [30, 31]. The red and cyan bands represent the result for NLO13 and the alternative version NLO19, respectively. The dotted line show the result for the Nijmegen NSC97f potential. (3) Calculation by the quark cluster model, that is, fss2 (solid curve) and FSS (dashed curve) [5].

In Figure 1.2, the total cross sections of the Λp elastic scattering are plotted with theoretical models such as the Nijmegen Extended Soft-Core (ESC) 16 model [10], the chiral Effective Field Theory (EFT) extended to YN sector [30, 31] and the quark cluster model [5]. In the low energy below 400 MeV/c, there exist several cross section measurements with hydrogen bubble chambers and these are the essential inputs to determine the S-wave contribution of the Λp channel. On the other hand, in the higher momentum range higher than 400 MeV/c, the cross section data were reported by one bubble chamber experiment and the total cross sections for each momentum region were determined from only $\sim$20 scattering events. Due to such limited statistics, there is no differential information such as differential cross section and spin observables.

The NN and YN interactions should be understood in a unified way using (broken) SU(3) symmetry. Table 1.1 shows the relationship between the isospin basis and the flavor SU(3) basis for the NN and YN channels with strangeness $S = -1$. These channels are related each other through the SU(3) flavor multiplet and ΛN and ΣN channels are discussed together theoretically. Now, the Σp scattering cross section data will be drastically updated by the E40 experiment. This should have theoretical impact even for the description of the ΛN interaction.

All theories predict the sizable cusp (enhancement) of the cross section at the ΣN threshold due to the strong $\Lambda N - \Sigma N$ ($I = 1/2$) $^3S_1 - ^3D_1$ coupling caused by the tensor force of

Table 1.1: The relationship between the isospin basis and the flavor SU(3) basis for the NN and YN with $S = -1$ channels

S	BB channel (I)	^1E or ^3O	^3E or ^1O
0	$NN(I=0)$	$--$	(10^*)
	$NN(I=1)$	(27)	$--$
	$\Lambda N(I=1/2)$	$\frac{1}{\sqrt{10}}[(8_s)+3(27)]$	$\frac{1}{\sqrt{2}}[-(8_a)+(10^*)]$
-1	$\Sigma N(I=1/2)$	$\frac{1}{\sqrt{10}}[3(8_s)-(27)]$	$\frac{1}{\sqrt{2}}[(8_a)+(10^*)]$
	$\Sigma N(I=3/2)$	(27)	(10)

the pion exchange potential. In the quark cluster model, the importance of the ALS which causes the $\Lambda N ^3P_1 - \Lambda N ^1P_1$ and $\Lambda N - \Sigma N(I=1/2) ^3P_1 - ^1P_1$ transitions is discussed because the additional ALS force due to the quark-quark interaction is predicted in the quark picture. Such ALS effect should appear in the Analyzing power (polarization) in the Λp scattering at this $\Lambda N - \Sigma N$ threshold region.

In the following subsection, we summarize the characteristics of several theoretical models

1.3.1 Nijmegen ESC model

Nijmegen extended-soft-core (ESC) models whose latest version is ESC16 [10], describe NN, YN and YY interactions in a unified way using broken SU(3) symmetry. The potentials consists of local and nonlocal potentials due to one-boson exchange which are the members of nonets of pseudoscalar, vector, scalar and axial-vector mesons, two psudoscalar exchange, meson-pair exchange and diffractive exchange. The meson-baryon coupling constants are calculated by imposing the SU(3) symmetry. In the Nijmegen model, there have been difficulties to reproduce the sufficiently repulsive short-range interaction in $\Sigma N(I=3/2,^3S_1)$ channel and $\Sigma N(I=1/2,^1S_0)$ channel which are explained quite naturally as the Pauli effect in the quark level in the (10) and (8_s) multiplets in the SU(3) representation in the quark level in the quark cluster model. In the latest ESC16 version, such "forbidden state" effect are taken into account phenomenologically by making an effective Pomeron potential as the sum of pure Pomeron exchange and of a Pomeron-like representation of the Pauli repulsion. The other difficulty was small LS splittings in the Λ hypernuclei which are characterized by the LS potential of $(V_{SLS} - V_{ALS})$ type. In conventional OBE model, ALS becomes smaller compared with SLS which leads the large LS splitting in the Λ hypernuclei. In this model, in order to reproduce the small LS splitting, some prescriptions have been performed such as meson pair exchange of the axial-vector pairs. These treatments of the ALS force should be tested with the Polarization (is equal to the Analyzing power) of the Λp scattering where the ALS and SLS should make a sizable contribution.

1.3.2 Quark cluster model

In the quark cluster model [5], the interaction Hamiltonian for quarks consists of the phenomenological confinement potential, the color Fermi-Breit interaction with explicit flavor-symmetry breaking, and the effective-meson exchange potentials of pseudoscalar, scalar and

vector mesons. The six quarks are put in the Gauss potential which is characterized by a size parameter b. These six quarks are imposed to be anti-symmetric under the exchange between any quark combination. The fermion nature of quark is taken into account and its effect is characterized the size parameter b. Large repulsive nature in the (10) and (8_s) multiplets in the SU(3) representation can be naturally predicted by the Pauli effect in the quark level. The color Fermi-Brit interaction between quarks gives another source of ALS, SLS and tensor forces in addition to the contribution from meson exchange potential. They predict the sizable ALS comparable to SLS and explain the small Λ hypernuclear LS splitting.

1.3.3 Chiral Effective Field Theory (Chiral EFT)

Chiral EFT has turned out to be a powerful tool for the derivation of nuclear forces. Its most notable feature is that there is an underlying power counting which allows one to improve calculations systematically by going to higher orders in a perturbative expansion. In addition, it is possible to derive two- and three- nucleon forces in a consistent way. This method is applied for the YN interaction and the ΛN and ΣN interactions are obtained at next-to-leading order where contributions from one- and two-pseudoscalar meson exchange diagrams and from four-baryon contact terms are considered [30, 31]. The chiral YN potential contains meson exchanges and a series of contact interactions with an increasing number of derivatives. For the former meson exchange, contributions from the pseudoscalar octet (π, K, η) are taken into account. The latter represent the short-range part of the interaction and are parametrized by low-energy constants (LEC), which need to be fixed by a fit to data. The present Chiral EFT framework is constrained from SU(3) symmetry in order to reduce the number of free parameter and there are five, eight and ten independent LECs for the S-waves at LO, the S-waves and S-D transition at NLO and for the P-waves at NLO. Even with such constraint, the number of the LEC parameters increases at the higher leading order. The present YN scattering data are insufficient to determine the LEC parameters higher than the next-leading order. One of the the most important experimental tasks is to provide higher precision data for the YN channels to impose the constraint to determine these parameters at NLO more accurately. Because the existing YN experimental cross sections are concentrated on the lower energy where the S-wave contribution is dominant, the experimental constraints for the P-wave parameters are quite weak. Therefore the differential cross sections and the polarization observables above $p_\Lambda > 400$ MeV/c are essential even for determining the LEC at NLO. At the NNLO, the number of LEC does not increase for the two-body interaction [32]. Therefore, accumulation of YN scattering data can contribute to extend Chiral EFT to NNLO.

Figure 1.3 shows the differential cross sections calculated by each model for the momentum range between 0.4 and 0.85 GeV/c. Two types of Nijmegen models (NSC97f and ESC16 [10]) and Jülich model [11] are presented as the typical example of the boson exchange picture. Two results by chiral EFT (chiral EFT13 [30] and 19 [31]) are calculated with the different sets of the LEC parameters both of which reasonably reproduce the YN scattering cross section. However, the strength of ΛN-ΣN coupling, which is closely related to the attraction in ΛN interaction in Λ hypernuclei, in chiral EFT13 is much larger than that in chiral EFT19. As for the total cross section, there are experimental data even for these momentum regions and the each model's parameters were determined to reproduce the existing total cross section. However the differential cross section in each model shows quite different angular

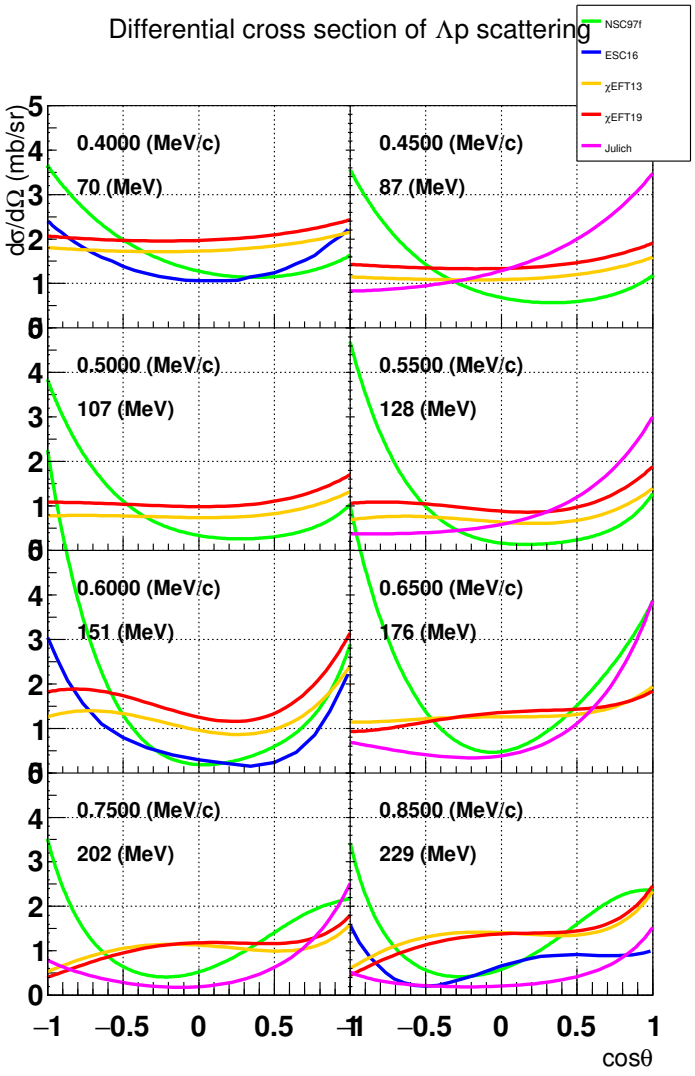

Figure 1.3: Differential cross sections calculated by theoretical models for the momentum range between 0.4 and 0.85 GeV/c. Two types of Nijmegen models (NSC97f and ESC16 [10]) and Jülich model [11] are presented as the typical example of the boson exchange picture. The two results by chiral EFT (chiral EFT13 and 19) [30, 31] are calculated with the different sets of the LEC parameters both of which reasonably reproduce the YN scattering cross section.

distribution due to the lack of the experimental input for the angular dependence. Such angular dependence might result from the higher-wave contributions and the charged kaon exchange in the Λp reaction for the backward scattering like the isospin exchange term in the np scattering. It is true that there were no experimental inputs to impose any constraint on such contributions. For this purpose, the accurate differential cross section data in the P-wave region are essential. The polarization measurements are also essential to determine the LS contribution which were never determined from the YN scattering data. Figure 1.4 shows the Analyzing power (Left) and the Depolarization (Right) for the polarized Λ beam [33, 34, 35]. In the lower momentum around 0.4 GeV/c where the P-wave contribution is less significant, there is no large model difference. However, the model difference appears clearly in the higher momentum region, where the P- and higher waves contribute in the reaction. Especially, the difference in the ΣN threshold (0.633 GeV/c for $\Sigma^+ n$ and 0.642 GeV/c for $\Sigma^0 p$) becomes significant due the different treatments of tensor force ($^3S_1 - ^3D_1$ transition) and ALS ($^3P_1 - ^1P_1$ transition). Such effect should be reflected in all measurements, that is, the differential cross section, Analyzing power and Depolarization.

In present, the experimental situation is changing. The J-PARC E40 experiment successfully detected the $\Sigma^+ p$, $\Sigma^- p$ elastic scatterings and the $\Sigma^- p \to \Lambda n$ reaction in the momentum range between 0.4 and 0.8 GeV/c. The differential cross sections for these channels will be derived in near future [26]. Such data are the first experimental inputs to impose the remarkable constraint on the theoretical models. As shown in Table 1.1, the ΛN and ΣN channels are related with each other through the flavor SU(3) representation. Because we measured both the $\Sigma^+ p (I = 3/2)$, $\Sigma^- p$ (superposition of $I = 1/2, 3/2$) elastic scatterings, the knowledge for all multiplets not included in the NN channels will be updated. Then, the theoretical prediction for the ΛN channel should become less uncertain compared with the present situation. It is worth comparing the experimental results of the Λp scattering with the updated theoretical calculations to test the theoretical framework with the flavor SU(3) symmetry.

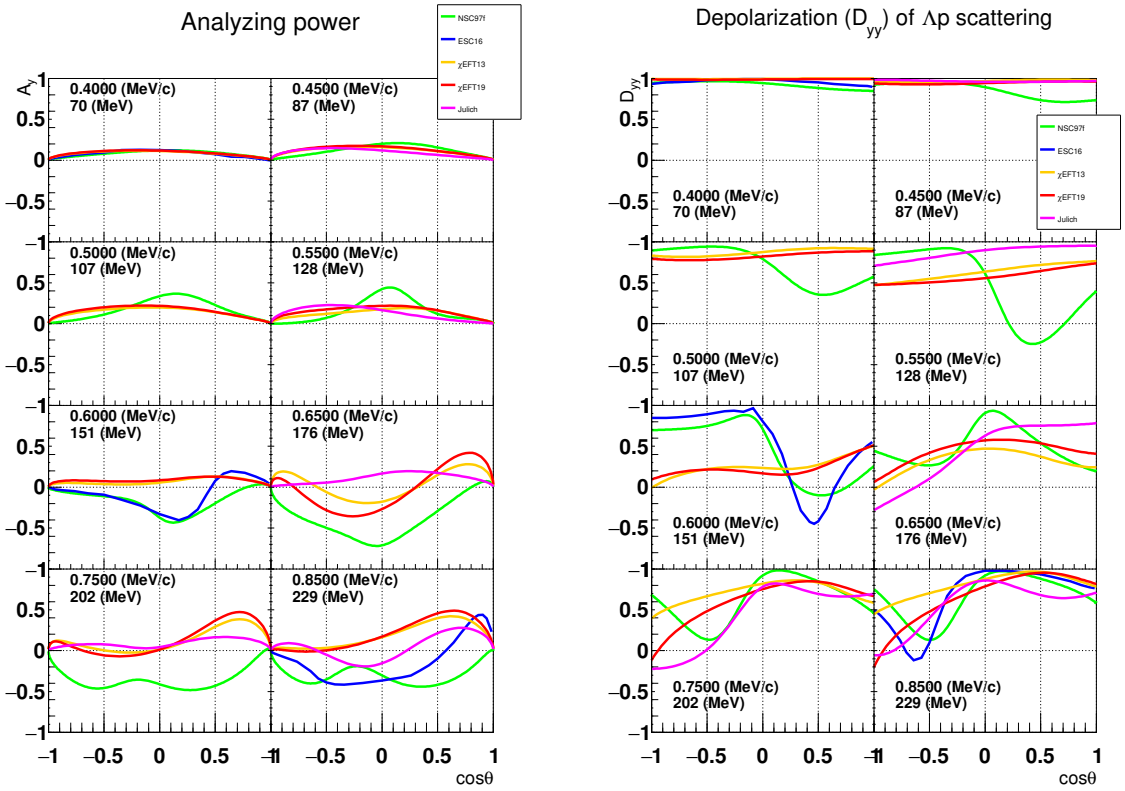

Figure 1.4: Theoretical calculation of the Analyzing power (A_y) (left) and the Depolarization (D_y^y) (right) for the polarized Λ beam. The each colored line is same with figure 1.3.

1.4 Impact on the neutron star physics

Hypernuclear physics are studied based on the two-body ΛN interaction, especially the Nijmegen models are widely used to study the hypernuclear structure. Due to the lack of the YN scattering data, such two-body models are partially tuned to reproduce the hypernuclear phenomena such as level splittings of Λ hypernuclei and Σ nuclear potential. In the last section, we have reviewed that there is a large disagreement among models even for the ΛN interaction which is intensively studied from Λ hypernuclei. The present urgent issue to be solved is the so-called "hyperon puzzle" in neutron star. This is the unsolved question how one can reconcile the softening of the equation of state (EOS) due to the appearance of hyperons with the observed two-solar-mass neutron star. Because Λ hyperon plays an essential role for the softening of the EOS, the understanding of the Λ potential in the high density region is indispensable. Currently, the importance of the three-body interaction including hyperon such as ΛNN is widely discussed.

Yamamoto *et al.* pointed out that such ΛNN three-body effect appears in the Λ binding energies in heavy Λ hypernuclei [36]. Two-body ΛN potential in the nuclei obtained by the G-matrix calculation from the Nijmegen ESC model was used. The three-body interaction, composed of the multipomeron exchange repulsive potential (MPP) and the phenomenological three-body attraction (TBA), is added as the density dependent potential. These three-body interaction's parameters were adjusted to reproduce the angular distribution of ^{16}O + ^{16}O elastic scattering at $E/A = 70$ MeV with use of the G-matrix folding potential, and values of the saturation density and the energy per nucleon there in nuclear matter. One of the possible scenarios to explain two-solar-mass neutron star is that such density dependent three-body repulsion (MPP) contributes additional repulsive force to support the gravity of the neutron star. Such three-body interaction should give a sizable contribution to the energy spectra of Λ hypernuclei. They calculated it systematically for wide mass number Λ hypernuclei ($^{13}_{\Lambda}$C, $^{16}_{\Lambda}$O, $^{28}_{\Lambda}$Si, $^{51}_{\Lambda}$V, $^{89}_{\Lambda}$Y, $^{139}_{\Lambda}$La, $^{208}_{\Lambda}$Pb) in the framework of the latest Nijmegen model (ESC16) with and without the three-body force as shown in Figure 1.5 where its energy spectra is reproduced well by including the three-body force [10]. They concluded that the density dependent three-body force works to reproduce better energy spectra of heavy system. In the high-density region, this three-body term dominated by MPP is expected to lead the stiff EOS of the hyperon-mixed neutron-star matter.

Isaka *et al.* also analyzed the Λ binding energies with the various Nijmegen two-body interaction models with AMD framework [37]. They pointed out that the three-body force strength reproducing the Λ binding energies depends on the two-body interaction model and there are considerable difference even within various ESC and NSC models. Such difference comes due to the potential of P-state contribution. Figure 1.6 shows the density dependence of the S- and P-state contributions to Λ potential as a function of k_F. In case of ESC14 which is similar to ESC16, the P-state contributions are small. On the other hand, in case of ESC12 and NSC96f, the P-state contributions are substantially repulsive. Therefore, in the former model, the Λ binding energies are well reproduced by adding the strong MPP repulsion which can support the two-solar mass neutron star. However, in the later model, the P-state repulsive contribution can reasonably work to reproduce the Λ binding energy and there is no room to introduce the strong MPP repulsion. The difference in the P-wave contribution even within the same Nijmegen framework is quite reasonable because these models predict the different behavior in differential cross section as shown in Figure 1.3. In the NSC97f, the larger P-wave contribution might make the differential cross section larger

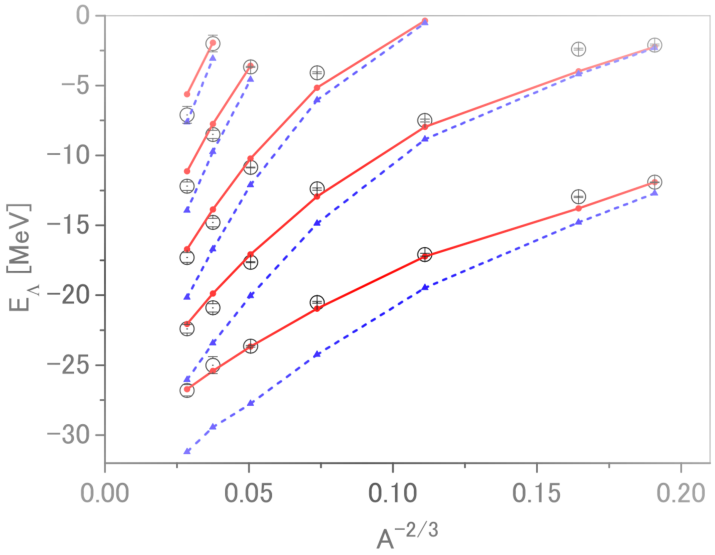

Figure 1.5: Energy spectra of ${}^{13}_{\Lambda}$C, ${}^{16}_{\Lambda}$O, ${}^{28}_{\Lambda}$Si, ${}^{51}_{\Lambda}$V, ${}^{89}_{\Lambda}$Y, ${}^{139}_{\Lambda}$La, ${}^{208}_{\Lambda}$Pb as a function of $A^{-2/3}$ calculated with the ESC16 model. Solid and dashed lines show calculated value by the G-matrix folding model derived from ESC16 with and without the three-body interaction, respectively. Open circles and error bars denote the experimental values.

than that in ESC16.

We believe that comparison between the high-resolution experimental data of the Λ binding energy and the Nijmegen model calculation with the three-body interaction is a crucial way to derive the ΛNN three-body interaction. In order to reinforce such the strategy, the accurate Λp scattering data are really awaited. In the NN sector, the realistic model of the nuclear force is established by updating the theoretical frameworks so as to reproduce a plenty of two-body scattering observables. Now, we also have to construct the realistic YN interaction model and both of theoretical and experimental efforts are necessary. For the experimental side, various scattering observables as many as possible with a reasonable precision should be measured as the basic information for constructiong a real bridge to the many-body system.

Chiral EFT is a promising theoretical framework to describe the nuclei and neutron matter. One of the biggest advantages of this model is that the three-body forces appear naturally and automatically in a consistent implementation of the framework. In the power counting in the present YN Chiral EFT, such three-body forces arise first at next-to-next-to-leading order ($\mathrm{N^2LO}$) in the chiral expansion [38]. If the decuplet baryons are included as explicit degrees of freedom, the three-body forces with decuplet excitation appear already at NLO. In this calculation, two types of B-M-B* and B*-B-B-B couplings appear where B, M and B* represent octet baryons, pseudo scalar mesons and decuplet baryons, respectively. The LECs in the B-M-B* coupling can be estimated through decuplet saturation [39]. The two-pion-exchange ΛNN [39] and ΛNN-ΣNN [40] forces are already applied to study a density-dependent effective potential for the BB interactions by integrating one nucleon degree of freedom in the medium. The repulsive effect of the ΛNN interaction is calculated to be about 5 MeV at normal density (ρ_0) and about 20 MeV at $2\rho_0$ in symmetric nuclear matter

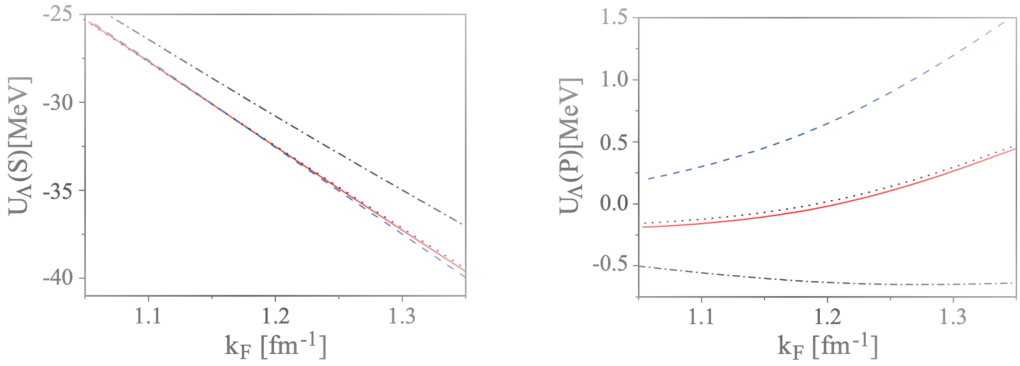

Figure 1.6: $S-$state (left) and $P-$state (right) contributions to U_Λ as a function of k_F. Red solid, blue dashed, black dotted, and black dot-sashed curves are for ESC14, ESC12, ESC08a, and ESC08b, respectively. The latest ESC16 is similar to ESC14.

[40]. A similar repulsive contribution is also obtained in pure neutron matter. The ΛNN-ΣNN coupling effect works to cancel the repulsive effect of the ΛNN interaction at normal density in symmetric nuclear matter. However, in the higher densities, the cancellation is incomplete and the net three-body force contribution is repulsive. In pure neutron matter, the effect of the ΛNN-ΣNN coupling effect is very small and, therefore, does not weaken the repulsion from ΛNN force[40]. In the present calculation, the three-body forces with B*-B-B-B couplings is not included yet, because there are two LECs which should be determined from experimental data. However, the number of LECs are limited. These parameters can be fixed from the 0^+ and 1^+ states of ${}^{4}_{\Lambda}$He[32]. A Λ-deuteron scattering experiment, which is also possible in future at J-PARC, can also contribute to fix these LECs. In general, such Λ-deuteron or Λ-α scattering measurement includes rich information to fix these LECs compared with the binding energy of a few-body hypernuclei. The structure of single-Λ hypernuclei is studied using the chiral EFT up to NLO by Jülich-Bonn-Munich group [41], where the three-body interaction is not included yet. A qualitatively good agreement with data is obtained for the chiral EFT19 interaction over a fairly large range of mass number values. This shows the potential of the chiral EFT model and it is worth providing scattering observables experimentally to update the chiral EFT model.

1.5 Goal of this experiment

We propose a new experiment to measure the differential cross section and spin observables (Analyzing power and depolarization) with a polarized Λ beam in the momentum range between 0.4 and 0.8 GeV/c at the K1.1 beam line. Λ beam is tagged by the $\pi^- p \to K^0\Lambda$ reaction at π^- beam momentum of 1.05 GeV/c. In this momentum, there are two experimental advantages. The first one is that the Λ production cross section becomes maximum (0.9 mb) in this beam momentum. The other one is that the produced Λ is polarized for the (π^-, K^0) reaction plane with almost 100% polarization. These features enable us to derive not only the differential cross section but also the spin observables. One of the experimental challenges is the identification of the $\pi^- p \to K^0\Lambda$ reaction, because the detection of $K^0 \to \pi^+\pi^-$ with an enough acceptance is not straightforward. However we have already

established the identification method of the $\pi^- p \to K^0\Lambda$ reaction with E40 by-product data which is described in Chapter 2.

The Λp scattering event is identified by the CATCH detector system, which were developed for the Σp scattering experiment, by detecting the scattered Λ and recoil proton. In this experiment, π^- from K^0 decay is also detected by CATCH as explained in next chapter. Experimental method is basically the same with one developed for the Σp scattering. A liquid hydrogen target is used as the Λ production and Λp scattering targets and the Λp scattering events are kinematically identified by detecting particles in the final state without any imaging information. High intensity π^- beam of 30 M/spill will be used to accumulate high intensity Λ beam. In Table 1.2, the experimental condition and the expected yield are summarized. In this experiment, we want to accumulate 100 M Λ beam in total with separated two periods. We request 34-days beam time including 29-days production run and 5-days commissioning and calibration runs as first stage to measure the differential cross section and the Analyzing power of the Λp scattering by accumulating 50M momentum-tagged Λ beam. As second stage, we request additional 34-days beam time including the production and commissioning/calibration runs with the same ratio to measure the depolarization and to improve the accuraces of measurements of the differential cross section and Analyzing power. Here, we assume that spill structure is 5.2 s cycle with a beam duration of 2 s and the π^- beam intensity is 30 M/spill.

The differential cross section is derived at least for four different momentum ranges (100 MeV/c momentum step) for 50M Λ beam as shown in Figure 1.7. The statistical error for angular region of $0 < \cos\theta < 0.1$ as a typical angular bin is expected to be 10% as listed in Table 1.2. In this simulation, Λp total cross sections for each momentum are assumed to be 15, 10, 20 and 12 mb, respectively, based on the past experimental data and theoretical calculation. The angular dependence is simply assumed to be flat for checking easily whether the analysis procedure works well or not. In the present analysis, we request two protons in the final state to suppress the background due to the background contamination in the Λ production identification. The angular acceptance for the differential cross section is limited due to this cut. We hope the angular acceptance becomes much wider by loosing the two-proton cut by improving the Λ identification method in future study. In this proposal, we are showing conservative but assured result in present study. As shown in Figure 1.7 for 50 M Λ beam, we can select best theoretical picture among the Nijmegen model (NSC97f and ESC16), Jülich boson-exchange model and chiral EFT(13 and 19) very clearly. In present, we are requested to select better model within the same theoretical framework (for example selection between chiral EFT13 and 19 or selection among NSC97f and ESC16 and other ESC versions). Selection of better model in the same theoretical framework could be possible even for 50 M Λ beam depending on the difference in the theoretical prediction. However, differential cross section measurement with narrower momentum step is quite effective to discriminate the better framework in the same theoretical model, because the momentum dependence of the differential cross section becomes quite large as shown in Figure 1.3 toward the Λ beam momentum of the ΣN threshold ($\sim$630 MeV/c) due to the tensor ${}^3S_1$-${}^3D_1$ coupling. Therefore, the differential cross section measurement with narrower momentum range of 50 MeV/c momentum step is very important to measure this momentum dependence. By accumulating 100M Λ beam in total, we will measure differential cross sections with 10% statistical error for each 50 MeV/c Λ beam momentum step from 0.4 to 0.8 GeV/c as shown in Figure 5.11 in Chapter 5. As mentioned in later, we need also 100M Λ beam for the D_y^y measurement.

Table 1.2: List of experimental condition and expected yield.

π^- beam intensity	30 M/spill (5.2 s cycle)
LH_2 target length	30 cm
Λ production cross section	0.9 mb
SKS acceptance for Λ production (w/ π^+ survival ratio)	0.58%
DAQ efficiency	90% (assumed)
Spectrometer analysis efficiency	80% (assumed)
K^0_S selection cut efficiency	80%
Tagged-Λ beam/spill	100
Tagged-Λ beam/day	1.72 M
Tagged-Λ beam with 29-days production run	50 M
Tagged-Λ beam with 58-days production run	100 M

CATCH efficiency	estimated value in E40 experiment
$d\sigma/d\Omega$ (Λp) $(0.4 < p$ (GeV/$c < 0.5))$	1.19 mb/sr (isotropic, 15 mb)
Λp scattering event for 50 M Λ beam	1580
dσ/dΩ stat. err at $0 < \cos\theta < 0.1$	14%
A_y stat. err at $0 < \cos\theta$ 0.2	17%
$d\sigma/d\Omega$ (Λp) $(0.5 < p$ (GeV/$c < 0.6))$	0.79 mb/sr (isotropic, 10 mb)
Λp scattering event for 50 M Λ beam	3200
dσ/dΩ stat. err at $0 < \cos\theta < 0.1$	10%
A_y stat. err at $0 < \cos\theta < 0.2$	11%
$d\sigma/d\Omega$ (Λp) $(0.6 < p$ (GeV/$c < 0.7))$	1.59 mb/sr (isotropic, 20 mb)
Λp scattering event for 50 M Λ beam	4900
dσ/dΩ stat. err at $0 < \cos\theta < 0.1$	9.7%
A_y stat. err at $0 < \cos\theta < 0.2$	11%
$d\sigma/d\Omega$ (Λp) $(0.7 < p$ (GeV/$c < 0.8))$	0.95 mb/sr (isotropic, 12 mb)
Λp scattering event for 50 M Λ beam	1100
dσ/dΩ stat. err at $0 < \cos\theta < 0.1$	22%
A_y stat. err at $0 < \cos\theta < 0.2$	24%

Table 1.3: D^y_y stat. error at $0 < \cos\theta < 0.2$ for 100 M Λ beam.

D^y_y stat. err at $0 < \cos\theta < 0.2$ for 100 M Λ beam	
$0.4 < p$ (GeV/$c < 0.5$)	25%
$0.5 < p$ (GeV/$c < 0.6$)	18%
$0.6 < p$ (GeV/$c < 0.7$)	13%
$0.7 < p$ (GeV/$c < 0.8$)	44%

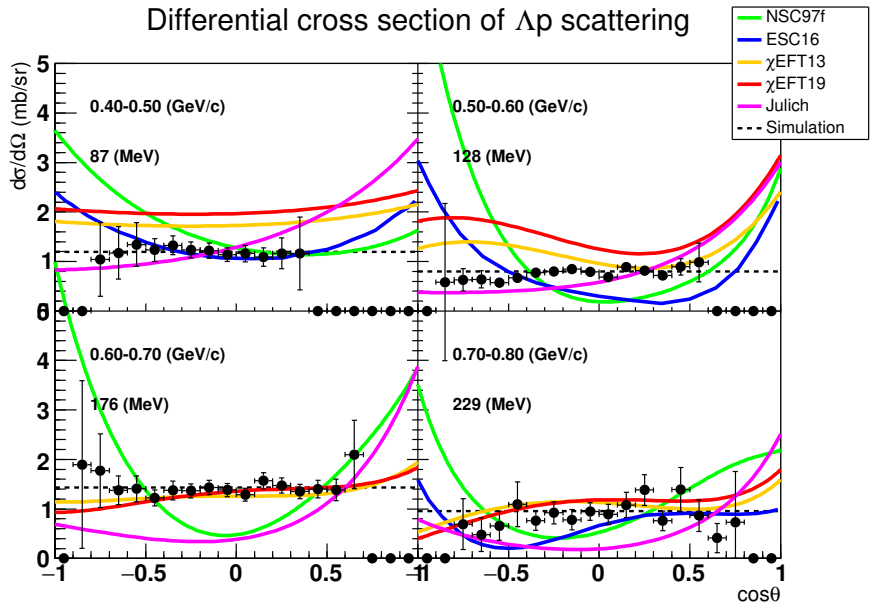

Figure 1.7: Simulated results for the differential cross section measurement of the Λp scattering in the momentum range from 0.4 to 0.8 GeV/c with 0.1 GeV/c momentum interval for 50M Λ beam. Theoretical calculations are also presented.

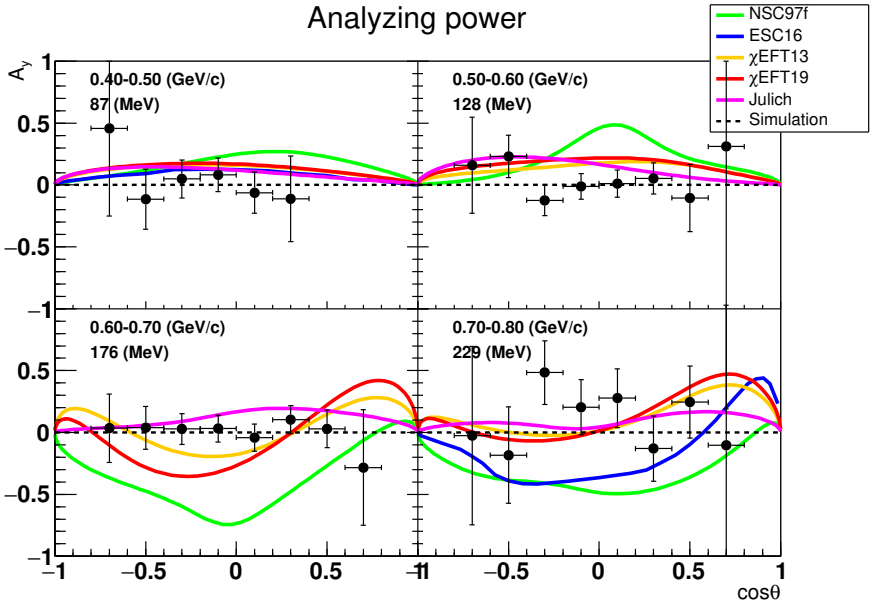

Figure 1.8: Simulated results for A_y measurement of the Λp scattering in the momentum range from 0.4 to 0.8 GeV/c with 0.1 GeV/c momentum interval for 50M Λ beam. Theoretical calculations are also presented.

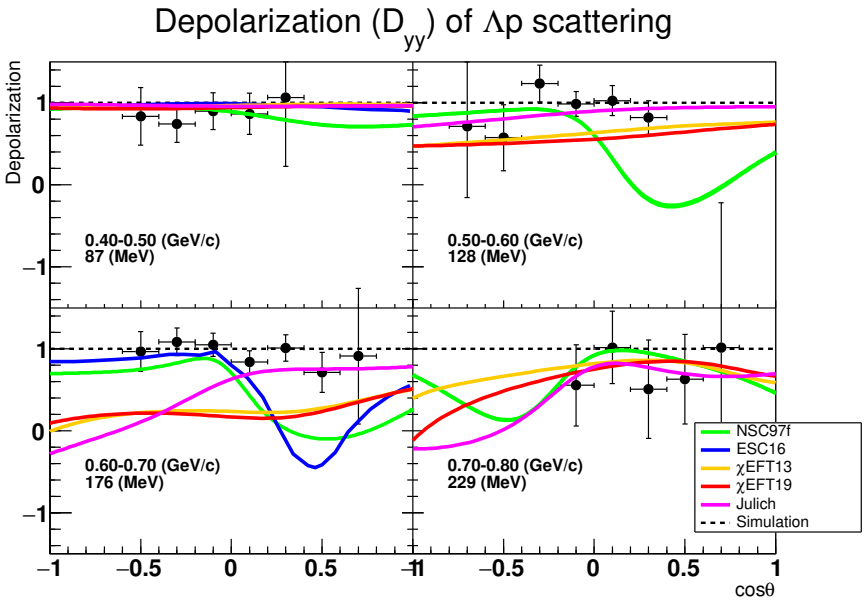

Figure 1.9: Expected D_y^y accuracy for 100M Λ beam. In this simulation, no spin transfer ($D_y^y = 0$) and no induced polarization ($P = 0$) in the Λp scattering are assumed for simplicity. The beam polarization of $P_\Lambda = 1$ is also assumed based on the past measurement. Theoretical calculations are also shown together. Due to the limitation of the statistics, errors in the high momentum region (0.7-0.8 GeV/c) are still large. However, in the middle momentum region (0.5 to 0.7 GeV/c) model difference between the chiral EFT and Nijmegen models can be clearly separated.

Figure 1.8 shows the sensitivity of Analyzing power (A_y) which were obtained from the left-right asymmetry for the Λp scattering for 50M Λ beam. The expected statistical error is about 10% for angular step of $d\cos\theta = 0.2$ as shown in Table 1.2. In this simulation, $A_y = 0$ is assumed to check the experimental validity easily. The normal technique used in the NN case where the beam polarization is flipped and the number of the scattered particle are counted with a single detector setup or the identical two detectors were placed in the left-right symmetric position, can not be used, because the Λ beam is produced in the tilted direction for the CATCH detector. Therefore the differential cross sections for the left scattered case and the right scattered case were derived and A_y is derived from these left- and right-differential cross sections as described in Section 6.2. We confirmed that A_y values were reasonably obtained by such analysis method in the simulation. In the momentum range higher than 0.5 GeV/c, there are large differences among three theoretical models. In order to discriminate these models, 10% accuracy is necessary and such new data are quite important to improve the theoretical models because sizable difference can appear in spin observables even thought the difference in the differential cross section is small. For example, there is large difference in A_y at 0.65 GeV/c between chiral EFT13 and 19, whereas there is very small difference in the differential cross section. A_y is sensitive for the anti-symmetric LS force (ALS). In the calculation by chiral EFT13, A_y values can be varied by adding ALS with a difference of 0.1 - 0.2 depending on the size of ALS [34]. Therefore the present accuracy of 10% is also necessary to constrain the ALS force from the A_y measurement. In Figure 6.9 in Chapter 6, the expected sensitivity for 100M accumulated Λ is also shown. By accumulating 100M Λ beam, the statistical error can be reduced to 8% level. The improved accuracy enables us to discriminate these theoretical models more clearly and to have a better understanding of ALS.

Figure 1.9 shows the simulated results for the depolarization (D_y^y) measurement for 100M Λ beam. For this measurement, the polarization of the scattered Λ has to be measured from the up-down asymmetry of the decay proton from Λ with respect to the scattering plane. The up-down symmetry in CATCH is rather better compared to the left-right symmetry because CATCH has the symmetric acceptance with respect to the central axis of the system. However, there are some detector asymmetry depending on the scattering vertex position and scattering angle. Such systematic effect due to the asymmetry in CATCH is also studied in this simulation. In this simulation, $D_y^y = 1$ which means no spin flip occurred in the scattering is assumed for the simplicity. We have confirmed the D_y^y can be reproduced reasonably by using the up-down asymmetry technique although there are some deviations due to the asymmetric effect. This is the first trial to measure the polarizations in both initial and final states and this is an important step to measure further measurements such as rotation parameters. As mentioned in Section 1.2, D_y^y is also the mixed combination of several spin-dependent and spin-independent amplitudes. However, D_y^y is expected to be closely related to the tensor force. Although the accuracy is very limited (15% level as shown in Table 1.3), the discrimination of theoretical models is possible for momentum range from 0.5 to 0.7 GeV/c as shown in Figure 1.9 . These data can also impose constraint on theories from different aspects. Accumulation of these spin observables and differential cross section are essential to improve these theoretical models and to establish the realistic YN interaction model in future.

This proposal is structured in the following. In chapter 2, we described the preliminary study of Λ identification method and possible Λp scattering identification using the E40 by-product data for the feasibility study. In chapeter 3, the experimental details for the newly

proposed experiment is described. In chapter 4, the simulation result for the $\pi^- p \to K^0 \Lambda$ reaction is described. In chapter 5, identification method of the Λp scattering is described and the derivation of the differential cross section is also mentioned. Finally, in chapter 6, the simulation for the spin observables is described.

Chapter 2

Preliminary study with E40 data

One of the biggest challenges for the Λp scattering is how the Λ production is identified with a proton target and charged meson beams. The well-established methods such as the (π^+, K^+) and (K^-, π^-) reactions convert neutron to Λ. In order to convert proton to Λ, the $\pi^- p \to K^0\Lambda$ reaction should be used. In this reaction, both π^+ and π^- from K^0_S should be detected. One idea to detect K^0 with a large acceptance is that π^+ and π^- are detected separately with different detector system, that is, π^+ is detected by the forward spectrometer and π^- is detected by the detector system surrounding the target. The E40 experimental setup was a typical example of such detector combination, that is, the forward magnetic spectrometer (KURAMA) for π^+ and CATCH for π^-. Therefore, at first, we analyzed E40 data where π^+ was detected by KURAMA as the background contamination of the $\pi^- p \to K^+\Sigma^-$ reaction [42].

2.1 Establishment of the $\pi^- p \to K^0\Lambda$ reaction

Main goal of the E40 experiment is to measure the differential cross sections of the $\Sigma^- p$ and $\Sigma^+ p$ scatterings by using $\Sigma^\pm$ beams produced by the $\pi^\pm p \to K^+\Sigma^\pm$ reactions. The E40 experimental setup is almost similar with the proposed experiment as shown in Figure 3.1 in next chapter. The forward magnetic spectrometer KURAMA was placed downstream of the target and the charged outgoing particles were momentum-analyzed and particle identification was performed. The liquid hydrogen target was surrounded by CATCH which consisted of cylindrical fiber tracker (CFT), BGO calorimeter and PiID for tracking, energy measurement and judgement whether the particle were stopped in the calorimeter, respectively. The idea how we identify K^0 is illustrated in Figure 2.1. The KURAMA spectrometer detects π^+ emitted to forward direction from K^0_S decay and its momentum is measured. Left figure in Figure 2.2 shows the relation between the squared mass and momentum of the particles detected by the KURAMA spectrometer. π^+ can be clearly identified. In coincidence with the π^+ detection by KURAMA, CATCH detected sideward-emitted π^- from the K^0_S decay. Because CATCH covered the whole azimuthal angle, a large acceptance was realized. Right figure in Figure 2.2 shows the ΔE-E relation between CFT and the BGO calorimeter in CATCH. Both π and proton can be identified. However, for the CATCH analysis, there are some uncertainties for the π measurement. First, its charge polarity of π can not be determined. Because the π^+ is detected by the forward spectrometer, the coincident π might be π^- for the charge conservation. Second, many of πs cannot be stopped in the BGO calorimeter and the energy information cannot be obtained for such events. Therefore the

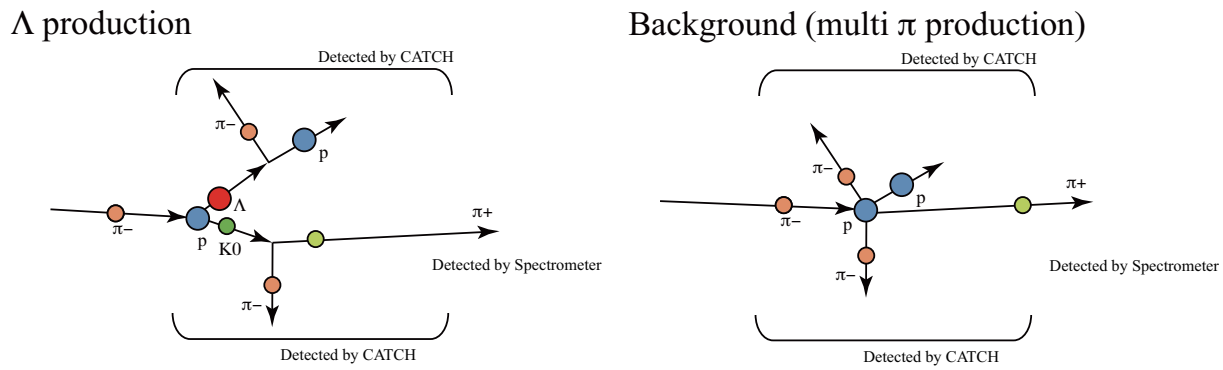

Figure 2.1: Conceptual drawing of detection method of the $\pi^- p \to K^0\Lambda$ reaction (left) and typical background with multi π production event without strangeness production (right). π^+ and π^- from K^0_S decay are separately detected by the forward spectrometer and CATCH.

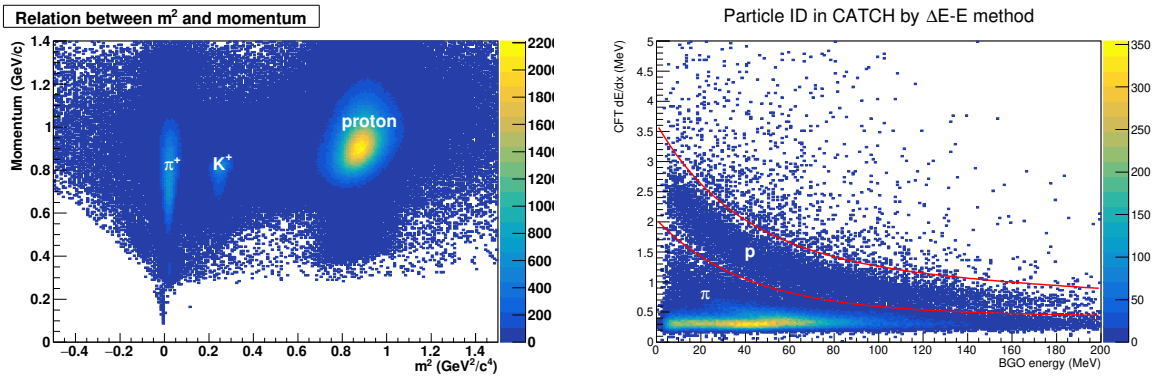

Figure 2.2: Particle identification for the KURAMA spectrometer (left) and CATCH (right). Left figure shows the relation between mass square and momentum for the KURAMA spectrometer and locus corresponding to π^+ is identified. Right figure shows the ΔE-E relation between CFT and the BGO calorimeter in CATCH. Proton and π can be identified. Be careful that many of πs cannot be stopped in the BGO calorimeter and the energy information cannot be obtained for such events.

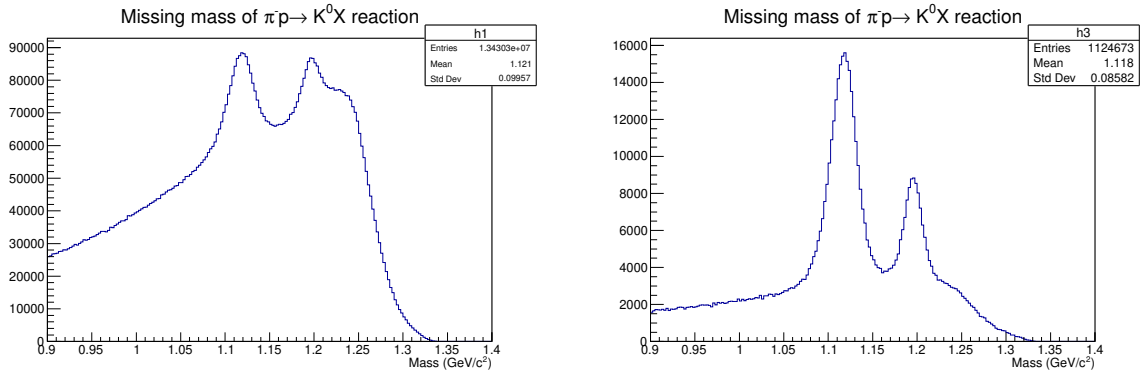

Figure 2.3: Missing mass spectra without and without K^0 selection cut for left and right figures, respectively. Peaks corresponding to Λ and Σ^0 can be identified, while the non-strangeness background events make a continuous background. In the right figure, the flight length cut was applied in order to improve the S/N ratio.

information for π^- is only the track direction. We need one assumption in this analysis. We assume that the pair of π^+ and π^- comes from the K^0_S decay and the momentum magnitude of π^- is calculated so that the invariant mass of $\pi^+\pi^-$ is equal to the K^0 mass. By imposing the assumption, the K^0_S momentum can be reconstructed by summing the momentum vectors of π^+ and π^-. Finally the missing mass spectrum of the $\pi^- p \to K^0 X$ reaction can be checked. Figure 2.3 shows the constructed missing mass spectra without and with K^0 selection cut for left and right figures, respectively. The K^0 selection cut is explained later. For the true K^0_S events, that is, the K^0 assumption is valid, the missing mass shows peaks corresponding to the $\pi^- p \to K^0 \Lambda$ and $\pi^- p \to K^0 \Sigma^0$ reactions. Of course, there are many background events which attribute to the multi-π event without strangeness production and such events make a continuous background in the missing mass spectrum. Even though such background contamination exists, it is an unexpected outcome that the Λ production can be identified significantly without any specific K^0 selection. The background for the K^0 events mainly come from the multi-π production event without strangeness production. In these events, all particles are emitted from the production vertex, whereas the K^0 decay vertex can be separated from the production point due to the K^0_S lifetime. Therefore by requesting that the decay vertex and the production vertex are separated, the S/N ratio can be improved as shown in Figure 2.3 (right). In this analysis, the vertex difference is required to be larger than 5 mm. However, about 60% of the produced K^0_S was rejected by this cut.

In this proposed experiment, the vertex resolution will be improved by installing the position detector just upstream of the target additionally. By utilizing the SKS spectrometer whose momentum resolution is about 10 times better than that of the KURAMA spectrometer, the missing mass resolution for Λ will also be improved.

2.2 Analysis of Λp scattering for the E40 data

In the E40 experiment, about 2.4×10^5 of Λ particles are identified without the K^0 selection cut although there are huge background due to the non-strangeness multi-π production. In this section, we describe the preliminary analysis to identify the Λp scattering events from these event samples. In order to identify the Λp scattering event, we check the kinematical

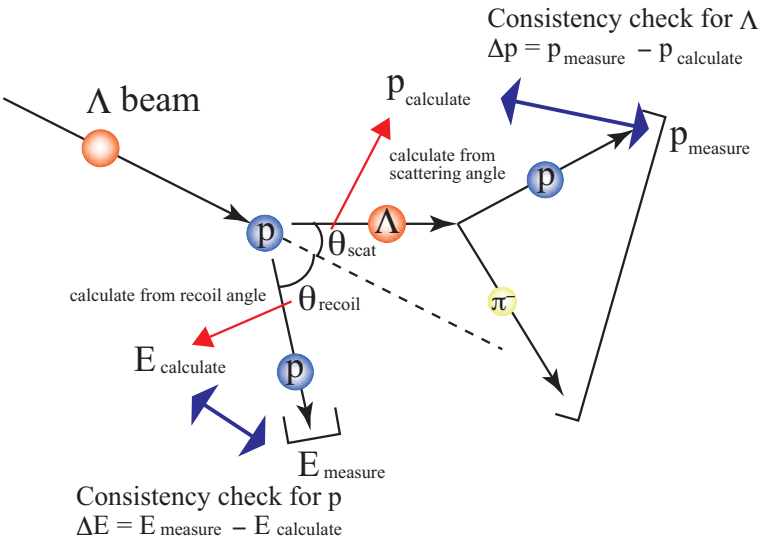

Figure 2.4: Conceptual drawing of the identification method of the Λp scattering. For the recoil proton, both the recoil angle (θ_{recoil}) and the kinetic energy are measured and the kinematical consistency between them is checked as the ΔE distribution. For the scattered Λ, the π^- momentum magnitude is determined so that the invariant mass of $\pi^- p$ becomes the Λ mass. Then the same kinematical consistency check between the scattering angle (θ_{scat}) and the reconstructed momentum is checked as the Δp distribution.

consistency between the angle and kinetic energy (or momentum) for the recoil proton and scattered Λ particle as shown in Figure 2.4. The momentum vector of the initial Λ beam is reconstructed from the spectrometer information. If the recoil proton is detected by CATCH, the recoil angle of proton can be obtained as the crossing angle between the Λ beam track and the proton track. The proton's energy can be calculated from the recoil angle of the proton by applying the Λp elastic scattering kinematics. Here, the calculated energy is described as $E_{calculated}$. On the other hand, the proton energy was measured by BGO and the measured energy is denoted as $E_{measured}$ here. Then we define $\Delta E(\Lambda p)$ as the difference between $E_{measured}$ and $E_{calculated}$, that is, $\Delta E(\Lambda p) = E_{measured} - E_{calculated}$, under the Λp elastic scattering assumption. If the recoil proton really originated in the Λp elastic scattering, such events would make a peak around $\Delta E(\Lambda p) = 0$ in the $\Delta E(\Lambda p)$ spectrum. If the pair of p and π^- is detected by CATCH, then the same kinematical consistency check is performed for the scattered Λ. The Λ momentum is reconstructed from the Λ decay where the momentum magnitude of π^- is determined so that the invariant mass of π^- and proton becomes the Λ mass. Then we check the consistency between the momentum magnitude and the scattering angle reconstructed with the Λ mass assumption. We also define $p_{measured}$ and $p_{calculated}$ as the measured momentum and the calculated Λ momentum from the scattering angle based on the Λp elastic scattering. Then $\Delta p(\Lambda p)$ is also defined as the difference between $p_{measured}$ and $p_{calculated}$, that is, $\Delta p(\Lambda p) = p_{measured} - p_{calculated}$. Like this, there are two indices to identify the Λp scattering. In order to suppress the background from the non-strangeness multi-π production such as $\pi^- p \to \pi^+ \pi^- \pi^- p$ event, two protons are required in the final state. Figure 2.5 shows the $\Delta p(\Lambda p)$ (left figure) and $\Delta E(\Lambda p)$ (right figure) spectra for the kinematical consistency checks for the scattered Λ and the recoil proton, respectively, for the E40 data. In both spectra, peaks at Δp (and ΔE) $= 0$ corresponding to the Λp

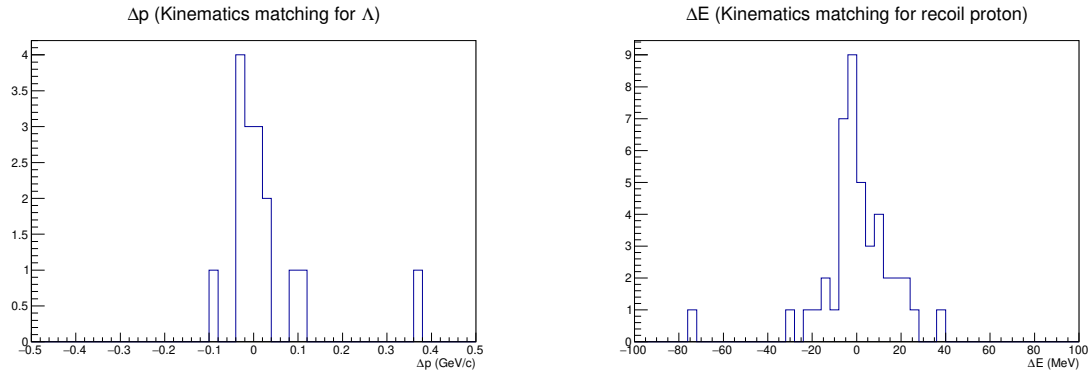

Figure 2.5: $\Delta p(\Lambda p)$ distribution for the scattered Λ (left figure) and $\Delta E(\Lambda p)$ distribution for the recoil proton (right figure). The peaks at $\Delta p(\Delta E) = 0$ correspond to the Λp scattering events.

scattering events are clearly identified. When all charged particles (π^- and two protons) are detected, both ΔE and Δp can be derived. In order to confirm the consistency of the Λp scattering identification, we also check the correlation between ΔE and Δp as shown in Figure 2.6. As expected, these events are confirmed as the Λp scattering events from both the recoil proton (ΔE) and the scattered Λ (Δp).

In the left figure in Figure 2.3 showing the identification of the initial Λ particle, there are many backgrounds. However, contributions from such background are well suppressed by selecting two protons in the final state and the Λp scattering can be clearly identified with smaller background structure in the $\Delta p(\Lambda p)$ and $\Delta E(\Lambda p)$ spectra. Therefore, the identification method of the Λp scattering is already established. We propose a new experiment dedicated to the Λp scattering.

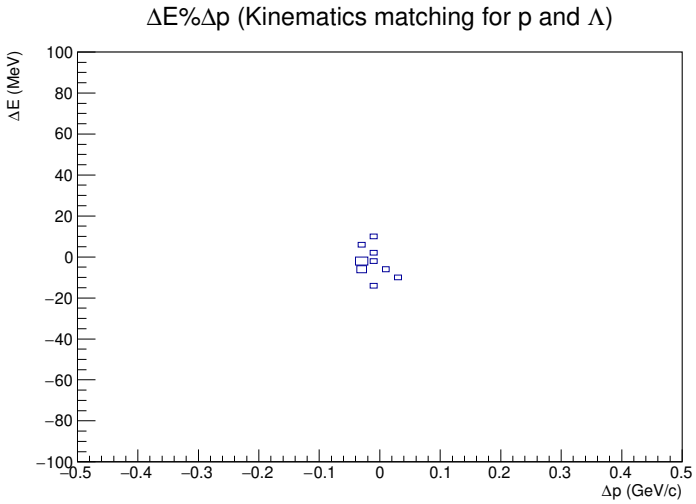

Figure 2.6: Correlation between $\Delta E(\Lambda p)$ and $\Delta p(\Lambda p)$ for events in which all charged particles are detected in the final state. Events are concentrated around $(\Delta p, \Delta E) = (0, 0)$ showing that these events are clear Λp scattering events from both kinematical indices.

Chapter 3

Λp scattering experiment at the K1.1 beam line

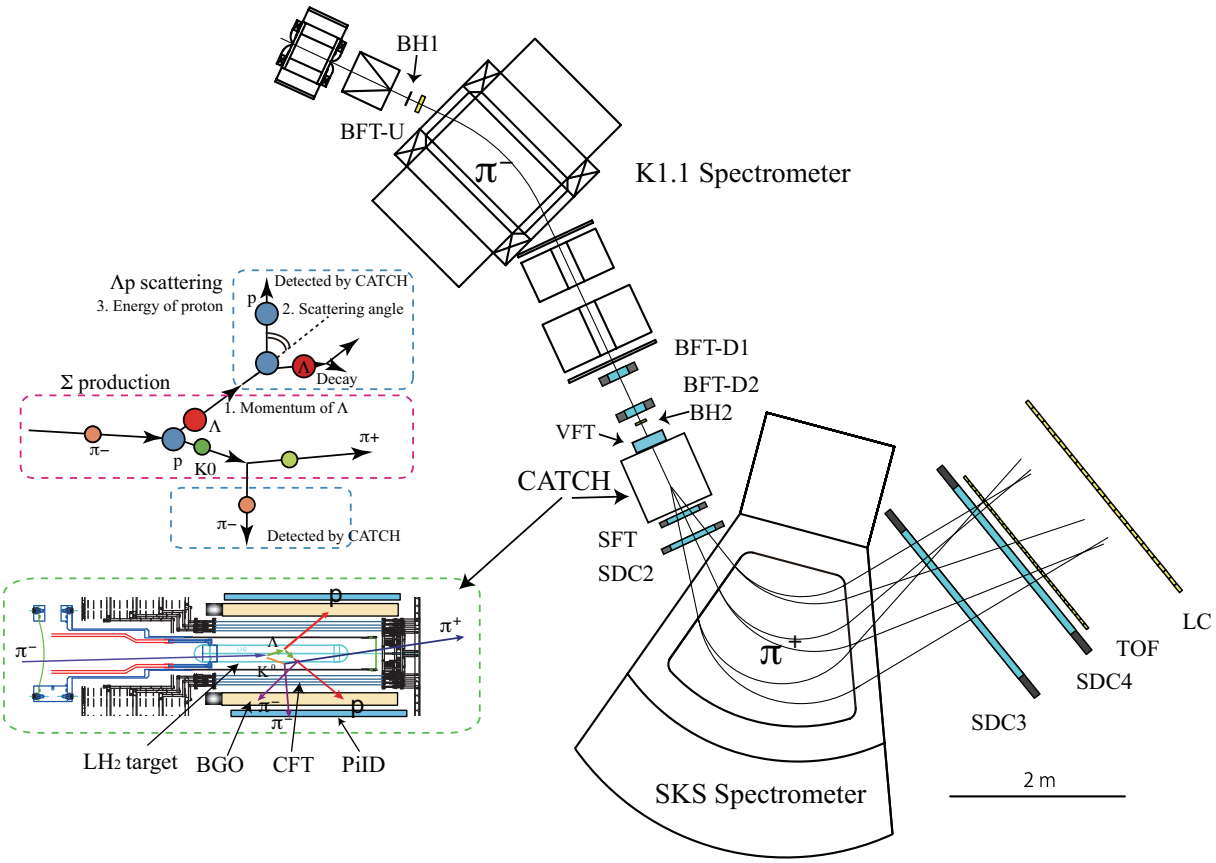

Figure 3.1: Experimental setup for the proposed Λp scattering experiment. The schematic drawing of how to identify K^0_S and Λp scattering is also shown.

We propose a new experiment for a Λp scattering by using a momentum-tagged Λ beam produced by the $\pi^- p \to K^0_S \Lambda$ reaction at the K1.1 beam line. Figure 3.1 shows the experimental setup. Experimental concept is almost the same with the E40 experiment for the Σp scattering. 1.05 GeV/c π^- beam is irradiated to the liquid hydrogen (LH_2) target with 30 cm thickness. We design experiment to use 30 M/spill π^- beam which is 1.5 times higher

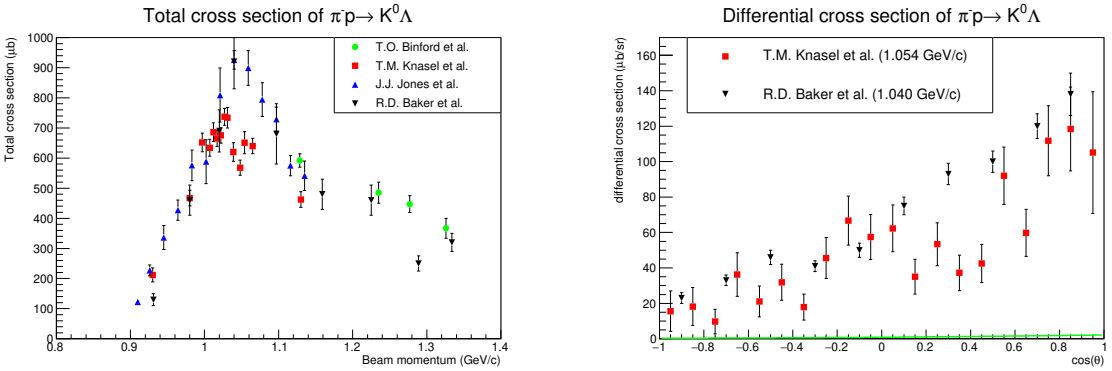

Figure 3.2: (Left) Momentum dependence of the total cross section of the $\pi^- p \to K^0\Lambda$ reaction. (Right) Differential cross section around p=1.05 GeV/c.

intensity than that in E40 in order to accumulate as much Λ beam as possible. The SKS spectrometer [43] is used as a forward spectrometer to detect π^+. Because the momentum resolution of SKS is expected to be $\Delta p/p = 10^{-3}$ (FWHM) which is 10 times better than that of KURAMA, the missing mass resolution for Λ will be improved and this also results in the improvement of the S/N ratio for Λ identification. In order to detect the Λp scattering and π^- from K^0_S decay, CATCH, which consists of a cylindrical fiber tracker, BGO calorimeter and PiID, is used as shown in enlarged figure in Figure 3.1. CATCH surrounds the LH_2 target and detect recoil proton and scattered Λ by detecting the $\pi^- p$ decay. In this section, we describe the experimental details.

3.1 Advantage of the $\pi^- p \to K^0\Lambda$ at $p_\pi = 1.05$ GeV/c

In order to realize the high-statistics Λp scattering experiment, it is quite important to accumulate as much Λ beam as possible. Therefore, the Λ production cross section is the one of the most important experimental parameters. Figure 3.2 (left) shows beam momentum dependence of the total cross section of the $\pi^- p \to K^0\Lambda$ reaction. The total cross section becomes maximum around ~900 μb at 1.05 GeV/c. Figure 3.2 (right) shows the differential cross section [44, 45, 46, 47]. There are two measurements that are not consistent with each other, but the measurement by R.D. Baker *et al.* [47] seems to be more reliable. In this simulation study, we have assumed that the Λ production cross section is 900 μb and the angular distribution by R.D. Baker *et al.* [47] are used.

Second important characteristics of this Λ production around 1.05 GeV/c is that Λ particles are produced with almost 100% polarization for the (π^-, K^0) reaction plane. Figure 3.3 shows the Λ polarization in the momentum range of $0.931 \leq p\,(\mathrm{GeV}/c) \leq 1.334$ measured by R.D. Baker *et al.* [47]. This polarization can be measured by the angular dependence of the proton from the Λ decay. As shown in this figure, the Λ polarization is sufficiently high. This high polarization is suitable to measure the spin observables. The detail of the Λ beam polarization is described in chapter 6. The K^0 angular region of $-0.2 < \cos\theta_{CM} < 1$ can be covered in the proposed setup, where θ_{CM} is the scattering angle of K^0 in the c.m. frame. Therefore almost 100% polarized Λ can be used as hyperon beam automatically. The production of the polarized Λ beam enables us to measure not only the differential cross section but also the spin observables such as Analyzing power (A_y) and depolarization (D^y_y).

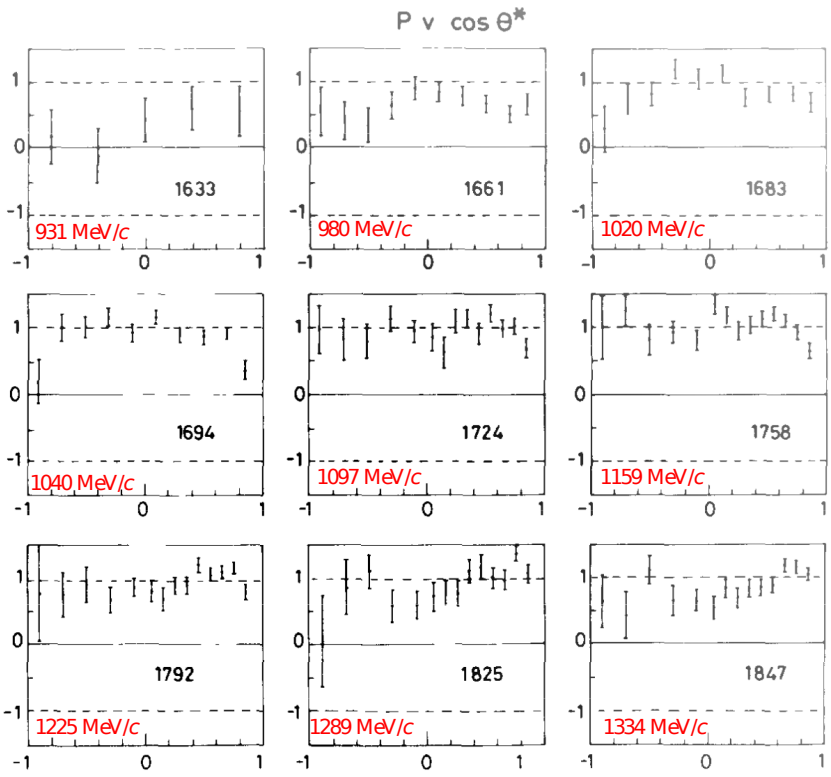

Figure 3.3: Induced polarization of Λ by the $\pi^- p \to K^0\Lambda$ reaction for $0.931 \leq p$ (GeV/c) ≤ 1.334. Horizontal axis shows $\cos\theta_{CM}$, where θ_{CM} is the scattering angle of K^0 in the c.m. frame. High polarization can be obtained for all momentum ranges.

3.2 The K1.1 beam line and beam line spectrometer

The K1.1 beam line is a new bam line which is proposed to construct in the existing hadron experimental facility and to be moved to the extended area after hadron hall extension project has been carried out. The K1.1 beam line is designed to provide a well-separated secondary charged K meson and π meson beams. The maximum beam momentum is 1.2 GeV/c. This momentum is designed for optimizing the $S = -1$ strangeness nuclear physics as already described in section 3.1.

The most downstream of the K1.1 beam line is the spectrometer part which consists of DQQ beam line magnet components and detector system, that is, the K1.1 beam line spectrometer. The momentum resolution is expected to be 3.8×10^{-3} in FWHM. As shown in Figure 3.1, the tracking detectors and timing detectors are placed upstream and downstream of the DQQ magnets for momentum analysis and particle identification, respectively. These detectors are required to work under the beam intensity of 30 M/spill. In the E40 experiment, we handled 20 M/spill beam with a detector setup which consisted of one layer of fiber detector and 12 layers of drift chambers of 3 mm wire spacing at the upstream and at the downstream of the spectrometer magnets, respectively, like the present setup. Because the drift chambers had the drift time of typical 30 ns, many tracks were reconstructed for one triggered event and sometimes we could not identify which beam track caused the reaction. In addition, sometimes the multiple signals during the drift time in the same wire made a

long-connected logic signal and information of the later signal was missing. Such multiple signal in the same wire resulted in the loss of the efficiency. Therefore, we are going to place 12 layers of fiber trackers (BFT-D) instead of drift chambers even for the downstream part of the spectrometer magnet. Then BFT-D can determine the beam timing with timing resolution of $\sigma = 1$ ns. Even for this fiber time gate of ± 3 ns for example, about 20% of beam particles makes multi track events. In order to select the true beam event, we request that the track is passing to the correct BH2 timing hodoscope segment, which has the 100 ps (σ) timing resolution.

In order to reconstruct the beam momentum, the reconstructed track at the downstream is inversely transferred to the upstream of the D magnet by using the transfer matrix and the beam trajectory is reconstructed to connect to the corresponding hit position at the single layer of upstream fiber tracker (BFT-U). The timing resolution for BFT-U is also about 1 ns (σ). Therefore about 40% of events have the multiple hit for BFT-U and this causes the uncertainty of the momentum reconstruction. In order to prevent from connecting between non-corresponding hits at the upstream and the downstream of the magnet, we request again that the reconstructed upstream track passes the true timing BH1 hodoscope segments with 100 ps timing resolution. The correspondence between BH1 and BH2 can be clearly identified with much better timing resolution under high counting rate. Therefore the selection of the true BH1 segment is not difficult. However in order to prevent multiple track event in the same BH1 segment, BH1 will be designed with a segment width of $\sim$5 mm and total segment number of about 45 to cover the beam spread about 200 mm. Under the high intensity beam condition, track reconstruction is performed with these techniques.

Another important point of beam particle analysis is the position resolution at the target to identify the flight length of K^0_S. Additionally, fiber tracker VFT1 will be installed just upstream of the LH_2 target with X and UV fiber configurations to determine both x and y positions of the beam.

3.3 SKS spectrometer

The SKS spectrometer is the well-established spectrometer system which was placed in the K1.8 beam line before. The SKS magnet was designed to achieve the momentum resolution of $\Delta p/p = 10^{-3}$ (FWHM) by bending the charged particle by 100 degrees. The trajectory of charged particle is reconstructed with the hit information of upstream position detectors (SFT and SDC2) and downstream position detecotr (SDC3, SDC4). The π^- beam does not penetrate the downstream detectors, because it is bent to the opposite direction for the positive scattered particles such as π^+. In the previous E40 experiment, the beam particle penetrated the downstream chambers and trigger counters. This caused the experimental difficulties for the operation of wire chambers and making trigger by counters. However, in the present experiment, it is not necessary to consider the operation under the high counting rate for the downstream detectors.

At the upstream, a fiber tracker (SFT) and a drift chamber (SDC2) will be placed. At the downstream, existing large drift chambers (SDC3 and SDC4) whose effective area is 2140 (H) $\times$ 1140 (V) mm^2 will be installed. The typical momentum of the π^+ from the K^0_S decay is rather low (0.3 - 0.75 GeV/c). The magnetic field is set to 0.5 T. The time of flight of the scattered particle is determined by the timing difference between the timing hodoscope at the beam line (BH2) and TOF wall at downstream. The typical flight length is 5 m. For

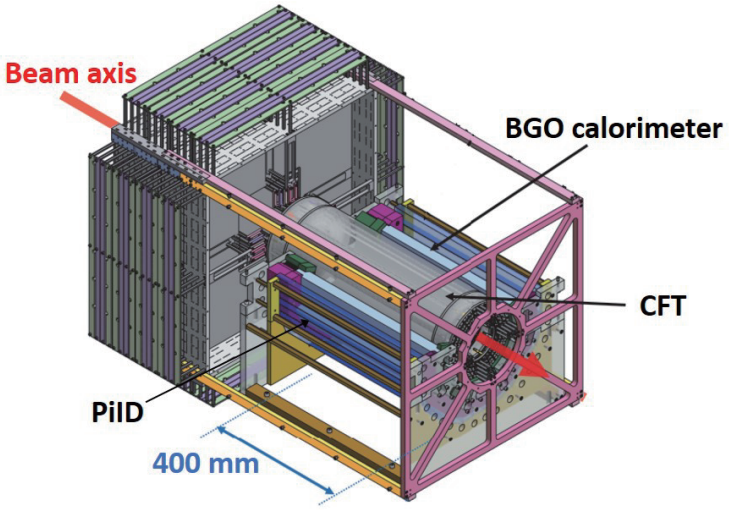

Figure 3.4: Figure of the CATCH system. CATCH consists of the Cylindrical Fiber Tracker (CFT) and the BGO calorimeter in order to measure the trajectory and the energy of emitted protons from the target installed inside of CATCH. PiID is used to check whether the recoil proton is stopped in BGO. The upper half of the BGO calorimeter and PiID is omitted in this figure.

the trigger purpose, Lucite cherenkov counter (LC) whose refractive index is 1.49 is placed in order to reject proton background in the trigger level. Another background source in the trigger level might be the beam reaction event at the SKS magnet. The beam is bent and stopped in the magnet with some reactions. This causes unexpected particles to the downstream detector. In order to reject such unexpected trigger, the hit-pattern matching between SFT, TOF and LC are required.

3.4 CATCH

CATCH is the cylindrical detector system developed for the previous Σp scattering experiment (E40). Figure 3.4 shows an illustration of CATCH, where the upper half of the BGO calorimeter and PiID is omitted to show the inner structure. CATCH is designed to have a cylindrical shape which surrounds the LH_2 target placed at the most inner position of CATCH. The LH_2 target with 20 mm radius and 300 mm thickness is already developed for E40 and the same target system will be used. CATCH consists of a cylindrical fiber tracker (CFT), the BGO calorimeter and the PiID counter for tracking, measuring the kinetic energy and checking whether the particle is stopped or not in the BGO calorimeter, respectively. CFT consists of 8 layers of cylindrical fiber layers whose radii are from 50 mm to 85 mm with 5 mm interval. CFT has two different layer configurations, that is, ϕ layer and uv layer. In the ϕ layer, scintillation fibers with a diameter of 0.75 mm are placed in parallel with the beam direction around the cylinder position. On the other hand, in uv layer, scintillation fibers with the same diameter are placed in spiral shape along the cylinder position and the u and v layers have the opposite tilt angle direction to the beam direction. CFT consists of 8 layers of these fiber configuration, that is , $u1, \phi1, v2, \phi2, u3, \phi3, v4$ and $\phi4$ layers. Then trajectories of charged particles from the LH_2 target are reconstructed three-dimensionally.

Photons from these scintillation fibers are detected by MPPC separately. In total ∼5,000 channels of MPPCs are read out and the timing and energy deposit information are obtained. BGO calorimeter is placed around CFT to measure the kinetic energy of the recoil proton by stopping in the calorimeter. BGO calorimeter consists of 24 BGO crystals whose size is 400 mm (l) × 30 mm (w) × 25 mm (t) and each BGO crystal is read out by connecting PMT at the downstream edge. Because BGO has a relatively long decay constant of about 300 ns, the pulse signal after an integrating circuit is read out by a flash ADC with a sampling interval of 30 ns to decompose the pile-up signals in the offline analysis. Finally, PiID counter, which consists of 32 segments of a scintillation counter, is placed in just outer side of the BGO calorimeter to check whether charged particle is stopped in the BGO calorimeter or not. The thickness of the BGO calorimeter is not sufficient to stop π^- and the hit information of PiID counter is used additionally to separate proton and pion in CATCH.

From the analysis of the E40 data, the performance of CATCH has been studied by using pp scattering data with several proton beam momenta from 0.45 to 0.85 GeV/c. The angular resolution of the CFT tracking is typically 1.3 degrees for proton. The energy resolution of BGO is expressed by the following equation,

$$\sigma(\mathrm{MeV}) = 0.5\sqrt{\frac{E(\mathrm{MeV})}{80}} + 4.0. \tag{3.1}$$

The detection efficiency of CATCH includes the acceptance of the detector, the tracking efficiency of CFT and the energy measurement efficiency of the BGO calorimeter. This depend on the angle and momentum of particle. The realistic efficiency was estimated with the pp scattering data where two protons were emitted. By identify the pp scattering event by detecting one proton, the other proton's angle and momentum could be predicted from the missing momentum of the $pp \to pX$ reaction kinematically. CFT tracking efficiency could be obtained by checking whether the predicted track could be detected or not. By using the pp scattering data with different incident beam momenta from 0.4 to 0.85 GeV/c, the momentum dependence of the recoil proton can be obtained. Figure 3.5 (left) shows the obtained efficiency map for the CFT tracking. The acceptance effect of CFT is also included in this efficiency map. The efficiency of the BGO calorimeter was also estimated by using the pp scattering. In this case, we checked whether the measured energy with the BGO calorimeter was consistent with the predicted energy from the pp scattering kinematics or not. Figure 3.5 (right) shows the obtained efficiency map for BGO. We have confirmed that the estimated BGO efficiency from data can be well reproduced by the Geant4 simulation. In the Λp scattering simulation, these realistic efficiencies are already taken into account. In the proposed Λp scattering experiment, the same calibration data of pp scattering should be collected for the CATCH efficiency measurement.

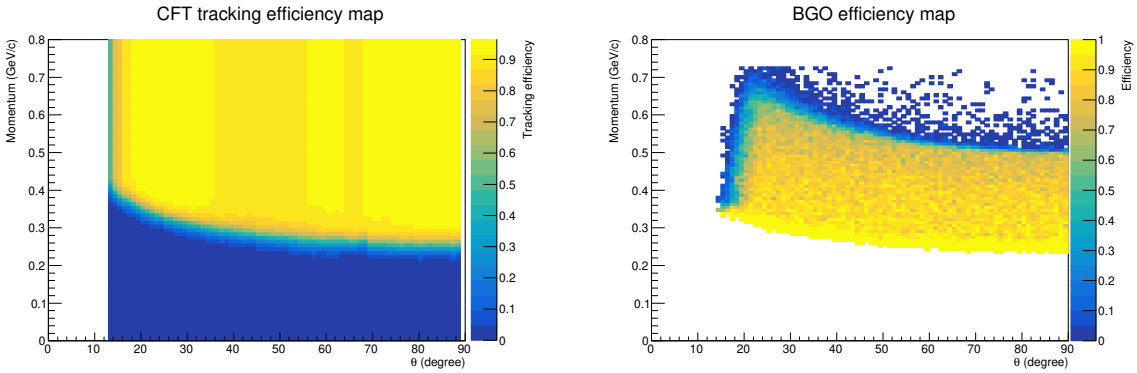

Figure 3.5: Estimated CFT tracking efficiency (left) and BGO efficiency (right) based on the *pp* scattering data and Geant4 simulation.

Chapter 4

Analysis of Λ production

We have already described how the $\pi^- p \to K^0 \Lambda$ reaction is identified, in Chapter 2. The same experimental method is also used in the proposed experiment. In this chapter, the expected missing mass spectrum is studied by taking into account both the realistic resolution and the realistic background contributions.

4.1 Identification of Λ

For the identification of Λ by the missing mass spectrum, π^+ and π^- from the K^0_S decay are detected by SKS and CATCH, respectively. The typical momentum range of π^+ is from 0.35 to 0.75 GeV/c. In such low momentum region, π^+ can be identified by SKS without any difficulties. The π identification by CATCH is already shown in Figure 2.2. Figure 4.1 shows the reconstructed missing mass with SKS by assuming the K^0_S invariant mass for the $\pi^+\pi^-$ for compensating the missing information of π^- momentum magnitude by CATCH. The missing mass resolution is improved to 5.8 MeV thanks to the good SKS momentum resolution.

In Figure 4.1, the expected background contribution is also shown. The background events are attributed to the multi-π production such as Δ productions. The cross sections for possible background reaction are listed in Table 4.1. From the reference data, the angular distribution for Δ production is almost flat in the c.m. frame and such realistic angular distribution is taken into account in this simulation. Among these background events, reactions involving the π^+ production becomes background in the missing mass. The Λ cross section of 0.9 mb is also used as the realistic value. In order to improve the S/N ratio more, we will apply the cut for the flight length of K^0_S, that is, the difference between vertices of the K^0_S decay and production. Figure 4.2 compares the vertex differences between for non-strangeness backgrounds (top figure) and for K^0_S events (bottom figure). The vertex difference (Δz) for the background makes a peak around $\Delta z = 0$, whereas that for K^0_S makes a tail structure toward the long distance direction due to the K^0_S lifetime. The background events can be rejected by 73% by requesting $\Delta z > 3$ mm with keeping the efficiency of 80% for K^0_S. The hatched spectrum in Figure 4.1 show the missing mass with the cut. This S/N ratio for the Λ identification is enough for the Λp scattering identification, because we already succeeded in identifying the Λp scattering event for the much worse S/N ratio in the E40 data.

The momentum of the produced Λ particle can be tagged from the missing momentum of the $\pi^- p \to K^0 X$ reaction. Figure 4.3 shows the momentum distribution of the momentum-tagged Λ particles which ranges from 0.4 to 0.8 GeV/c.

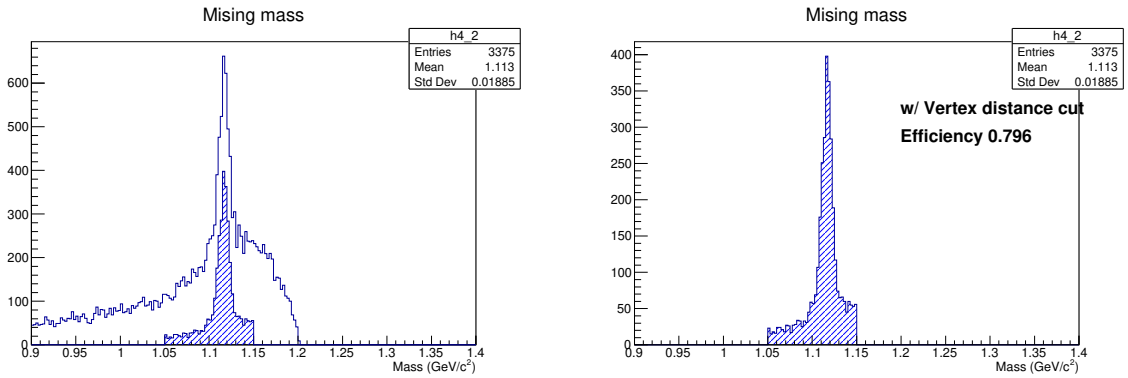

Figure 4.1: Missing mass spectra for the $\pi^- p \to K^0 X$ reaction with K^0 invariant mass assumption. The left figure and hatched spectrum in the right figure show the missing mass after the K^0_S flight length cut.

Table 4.1: Cross sections for the $\pi^- p$ reaction for different final states. The branching ratio for the intermediate state is also listed from the reference. Values which were not found in reference are described as "assumed".

Reaction	Cross section	Ratio
$\pi^- p \to \pi^- p$	~28 mb	
$\pi^- p \to \pi^0 n$	~3.5 mb	
$\pi^- p \to \pi^- \pi^+ n$	~10 mb	
$\pi^+ \Delta^-$		57.6%
$\pi^- \Delta^+$		7.2%
$\rho^0 n$		0.3%
phase space		34.9%
$\pi^- p \to \pi^- \pi^0 p$	~7 mb	
$\pi^- \Delta^+$		60% (assumed)
phase space		40% (assumed)
$\pi^- p \to \pi^0 \pi^0 n$	~2 mb	
$\pi^- p \to \pi^0 \pi^0 \pi^0 n$	~0.5 mb	
$\pi^- p \to \pi^+ \pi^- \pi^- p$	~2.5 mb (assumed)	

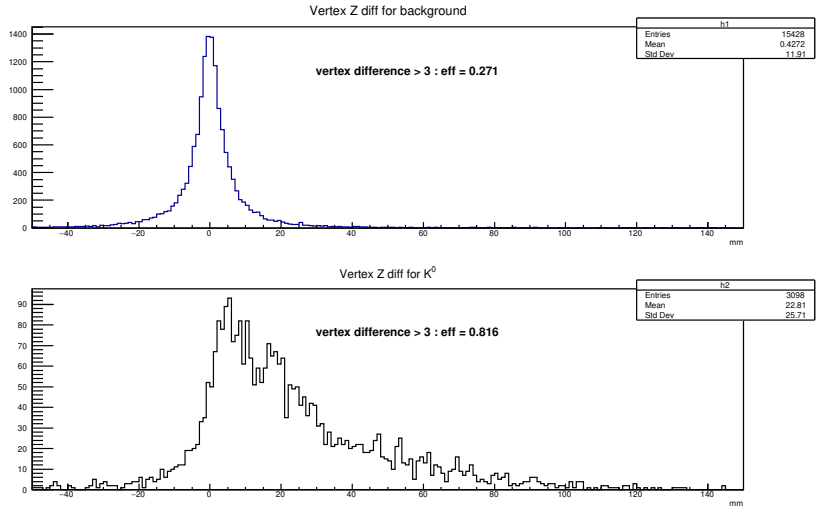

Figure 4.2: Vertex difference between vertices of decay and production for non-strangeness backgrounds (top) and for K^0_S events (bottom).

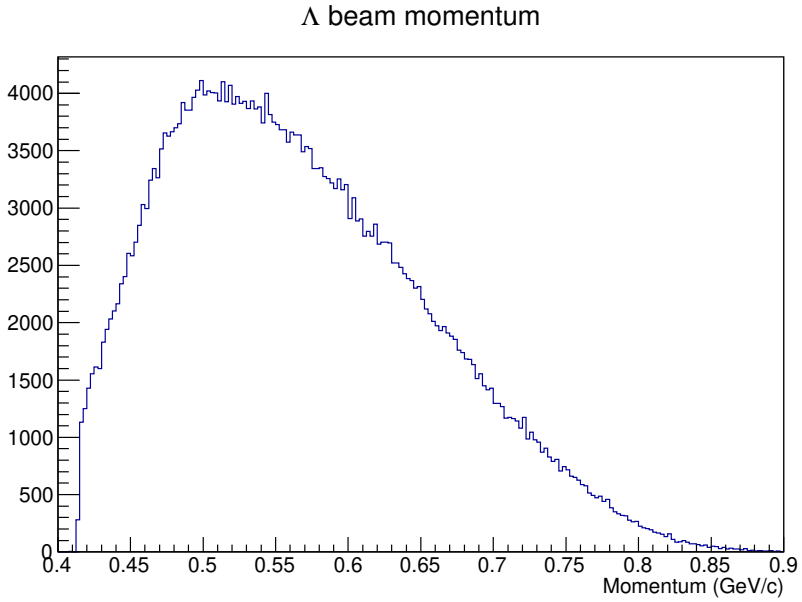

Figure 4.3: Λ beam momentum distribution reconstructed as the missing momentum of the $\pi^- p \to K^0 X$ reaction.

Table 4.2: Expected trigger rate for the (π^-, π^+) reaction. These trigger rates are estimated based on the production cross section and spectrometer acceptance.

Reaction	Cross section	Trigger number (/spill)
$\pi^- p \to \pi^+ \Delta^- \to \pi^+ \pi^- n$	$\sim$5.7 mb	2,160
$\pi^- p \to \pi^- \Delta^+ \to \pi^+ \pi^- n$	$\sim$0.72 mb	550
$\pi^- p \to \pi^+ \pi^- n$ (phase space)	$\sim$3.5 mb	1,590
$\pi^- p \to \pi^- \Delta^+ \to \pi^- \pi^0 p$	$\sim$4.2 mb	0
$\pi^- p \to \pi^+ \pi^- \pi^- p$	$\sim$2.5 mb (assumed)	375
Background total		$\sim$4,600
$\pi^- p \to K^0 \Lambda$	0.9 mb	180

4.2 Λ yield and trigger rate

Table 4.2 shows the expected trigger rate of the (π^-, π^+) trigger by taking into account the SKS acceptance. The trigger rate is estimated to be 5k /spill. In the E40 experiment, the DAQ efficiency of 90% was obtained for 8k/spill trigger request. Therefore, these trigger rate can be manageable.

The Λ yield of 180 per spill for 100% efficiency is also shown in Table 4.2. We assume the following efficiency,

- DAQ efficiency : 90%,
- Spectrometer analysis efficiency 80%,
- K^0_S selection cut efficiency 80%.

The momentum-tagged Λ particle is estimated to be about 100 per spill for 30 M/spill π^- beam intensity. Assuming that the spill structure is 5.2 s cycle with a beam duration of 2 s, the accumulated Λ beam is expected to be 1.72 M per day. We are considering that 50M Λ beam is necessary for the differential cross section and the analyzing power. In order to measure the depolarization, 100 M Λ beam is necessary. These numbers of the Λ beam correspond to the beam times of 29 days and 58 days, respectively.

Chapter 5

Analysis of differential cross section of Λp scattering

5.1 Kinematical identification of Λp scattering events

In this section, we review how Λp scattering events are identified from the CATCH information. Figure 5.1 shows the event category of proton event in the final state in coincidence with Λ production in the LH_2 target. The Λp scattering event is of our interest. In order to identify the Λp scattering event, we request at least two protons to be detected in CATCH to mainly suppress the background events such as non-strangeness background in the Λ production and Λ decay. If the identification of the Λ production becomes more clean, the analysis with two charged particle (proton and π^- or two protons) would be possible. In this study, to obtain the assured result, we required two protons in this simulation. At first we describe how Λp scattering events are identified from the CATCH information. In the next section, we describe how such background events are separated from the Λp scattering events.

For the identification of the Λp scattering events, we check whether detected energy of recoil proton or scattered Λ is consistent with the expected energy from the scattering angle based on the Λp elastic scattering kinematics as already described in Chapter 2. When the proton is detected by CATCH, its kinetic energy and the recoil angle are obtained from energy measurement by the BGO calorimeter and tracking by CFT, respectively. Then,

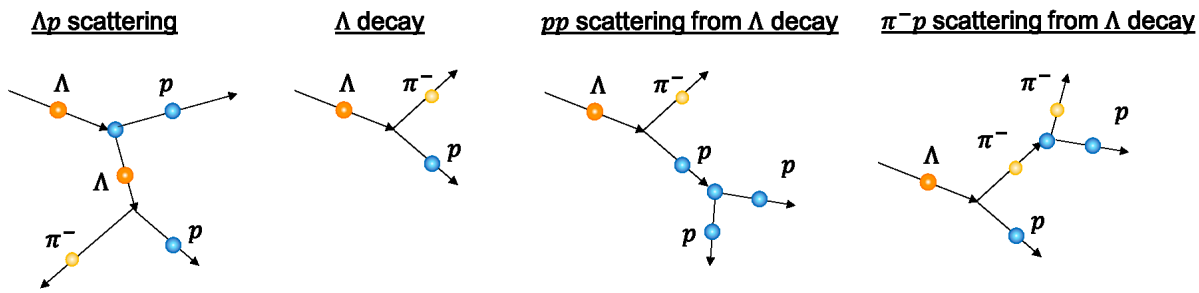

Figure 5.1: Event category of proton event in the final state in coincidence with Λ production in the LH_2 target. In addition to the Λ decay, secondary scattering of the decay products becomes background where protons are emitted in the final state.

we can calculate the expected kinetic energy of proton from the recoil angle based on the Λp elastic scattering kinematics. We denote this calculated proton's kinetic energy and the measured one by the BGO calorimeter as $E_{calculate}$ and $E_{measure}$, respectively. We require the energy difference, that is, so called ΔE to be zero within the experimental resolution.

The proton is also emitted from the Λ decay. Therefore when π^- is detected with proton, we also check the kinematical consistency assuming that the proton-π^- pair is the scattered Λ. As we already mentioned, many of π^-'s are not stopped in the BGO calorimeter. We have to determine the π^- momentum magnitude with some kinematical assumption. Here, we assume the proton-π^- pair comes from Λ decay and we request that the invariant mass of the proton-π^- pair should be the Λ mass. By imposing this assumption, the π^- momentum can be obtained. Then the Λ momentum which is denoted as $p_{measured}$ can be reconstructed as the sum of momentum vectors of the proton-π^- pair. We again check the kinematical consistency between the calculated momentum from the scattering angle ($p_{calculate}$) and measured momentum ($p_{measured}$). The difference between two momenta, that is, Δp is required to be zero within the experimental resolution. This method is already used in the E40 analysis to identify the $\Sigma^- p \to \Lambda n$ reaction.

For the proton, there is two possibilities, that is, recoil proton and scattered Λ decay. When proton and π^- are detected, we calculate both ΔE and Δp assuming the possibilities of the recoil proton and scattered Λ, respectively, and we select more likely combination by comparing ΔE and Δp .

5.2 Identification of background for the Λp scattering

As shown in 5.1, the main backgrounds for the Λp scattering are Λ decay and the secondary reaction of the Λ decay products with the LH_2 target. In this simulation, these secondary reactions such as pp, np and $\pi^- p$ are taken into account based on these cross sections. np scattering by the neutron from $\Lambda \to \pi^0 n$ decay cannot be identified. However there is no significant effect from np scattering for the final ΔE and Δp spectra because at least two charged particles are requested. Other backgrounds are basically identified by using the CATCH information and we explain this procedure in the following subsections.

5.2.1 Rejection of pp scattering after Λ decay

In the $\Sigma^- p$ scattering in E40, the np and $\pi^- p$ background from the $\Sigma^- \to \pi^- n$ decay could be clearly identified by the identification method described here. pp scattering is the main background in coincidence with the Λ production because $\pi^- p$ scattering cross section is much smaller than that of pp scattering. This situation is same with E40 where the np scattering is much larger than $\pi^- p$ background.

When π^- is detected by CATCH, at first, we assume that this π^- is emitted from the Λ decay. Then, the π^- momentum magnitude can be calculated from the emission angle of π^- from the Λ decay kinematics. Momentum vector of corresponding decay proton can be calculated from the momentum conservation in the Λ decay. Such momentum-tagged proton is regarded as proton beam. We assume proton detected by CATCH is the recoil proton by the pp scattering and we make $\Delta E(pp)$ plot, where the difference between the measured proton energy ($E_{measure}(pp)$) and calculated proton energy from proton angle assuming pp scattering ($E_{calculate}(pp)$) is filled. Figure 5.2 shows the $\Delta E(pp)$ plots for four Λ

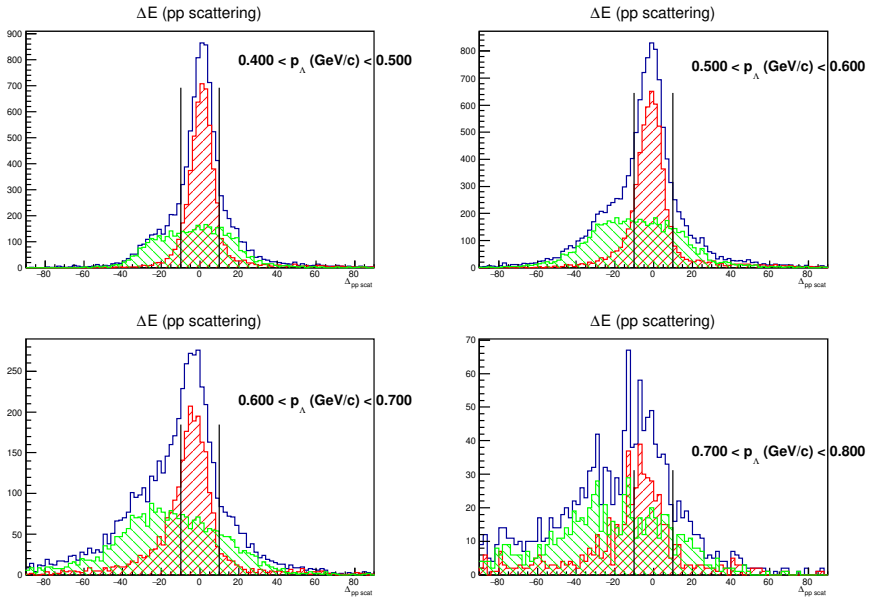

Figure 5.2: $\Delta E(pp)$ plot assuming pp scattering for four Λ momentum regions with 100 MeV/c interval. The open histogram shows the contribution including all reactions. The red and green histograms show the contribution from pp scattering and Λp scattering, respectively.

momentum regions with 100 MeV/c interval. pp scattering event (red histogram) makes a peak around $\Delta E(pp) = 0$ whereas Λp scattering event (green histogram) makes broad distribution. Because the pp cross section decreases with proton beam energy, the contribution of pp scattering becomes less significant at the higher Λ beam momentum region. In order to reject the pp events, we set cut region for the $\Delta E(pp)$ as shown by lines in Figure 5.2 and these events are removed even though some of Λp scattering events are also removed. The efficiency for the Λp scattering events are estimated as shown in Figure 5.3. This cut efficiency depends on the Λ beam momentum and the scattering angle and is taken into account in a total efficiency of analysis in the derivation of the differential cross section.

5.2.2 Identification of Λ decay event

Proton from Λ decay is the biggest background contribution. The single proton events is suffered from this decay background. Therefore by selecting at least two proton events, such decay event can be almost 100% suppressed. However, these Λ decay events could remain as a possible background source. Here, we describe how these decay protons can be identified and be suppressed by detecting pair of $\pi^- p$. In case that π^- and proton are detected, this decay event can not be distinguished from the Λp scattering event at 0 degree. Therefore, the Λ decay events are identified as the Λp scattering event at 0 degree as shown in Figure 5.4 where relation between the scattering angle ($\cos\theta$) and Δp are plotted. The decay events concentrate at ($\cos\theta$, Δp) = (1, 0). Because the decay events are huge compared with the scattering events, the Λp scattering events at the very forward angle $\theta \sim 0$ can not be distinguished from the Λ decay. If we perform the recoil proton analysis (ΔE) for the decay proton, such decay events make a background locus around $\cos\theta < -0.8$ as shown in Figure

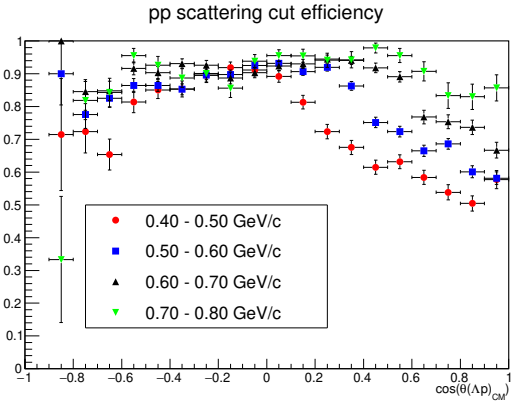

Figure 5.3: The efficiency of the pp rejection cut for the Λp scattering events for each momentum region.

5.5. In the analysis of the π^- and proton final state, we will suffer from this decay background around these angular region even though many of the Λ decay events are rejected by the Δp analysis. Therefore the accuracy of the differential cross section around these angle region will be worse than other angular region.

5.3 Identification of Λp scattering

Λp scattering events are identified by checking the kinematical consistency between the energy and the scattering angle for the scattered Λ (Δp) and the recoil proton (ΔE), respectively, as described in Section 5.1. In this simulation study, we apply the background cuts described in Section 5.2 to improve the S/N ratio. The realistic CATCH efficiency obtained from the E40 analysis is used. For the scattered Λ, the branching ratio of the $\Lambda \to \pi^- p$ mode is taken into account. Figure 5.6 and Figure 5.7 show two-dimensional plots between the scattering angle ($\cos\theta$) and Δp for the scattered Λ and ΔE for the recoil proton, respectively, after the background rejection cuts. The locus at $\Delta p = 0$ corresponds to the Λp scattering event. Similarly, the Λp scattering event at $\Delta E = 0$ can be clearly identified. The angular acceptance is mainly determined by the detection efficiency for two protons. Figure 5.8 shows the scattering angle dependence of the detection efficiencies for the scattered Λ and the recoil proton for each momentum region. In this efficiency estimation, the two-proton cut is not included to show the angular acceptance for recoil proton and scattered Λ separately. Detection of very low-energy proton is difficult. In the backward angular region in Figure 5.8, the proton energy from Λ decay is too small to detect it. The situation is the same for the recoil proton in Figure 5.8. In the forward angular region (of Λ), the energy of the recoil proton is too small to detect it and the Λp scattering event can not be identified from the recoil proton analysis. Because we request two protons, angular acceptance for both forward and backward regions are limited in both Δp and ΔE spectra in Figure 5.6 and 5.7. However, if the analysis of only $\pi^- p$ pair is possible, almost all scattering angle can be covered by merging the both analyses for the scattered Λ and the recoil proton. For this purpose, the Λ identification with less background is a key to realize this analysis.

Figure 5.9 shows the projected Δp and ΔE spectra. In each momentum region, the

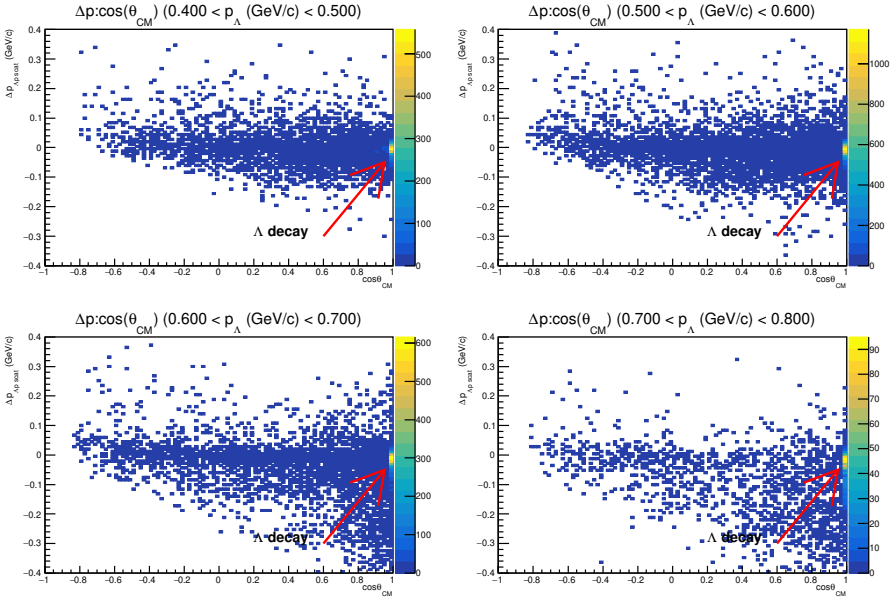

Figure 5.4: Correlation between the scattering angle ($\cos\theta$) and Δp for the scattered Λ analysis. Because the Λ decay can be seen as the Λp scattering at 0 degree. Therefore, the Λ decay events concentrate at ($\cos\theta$, Δp) =(1, 0);

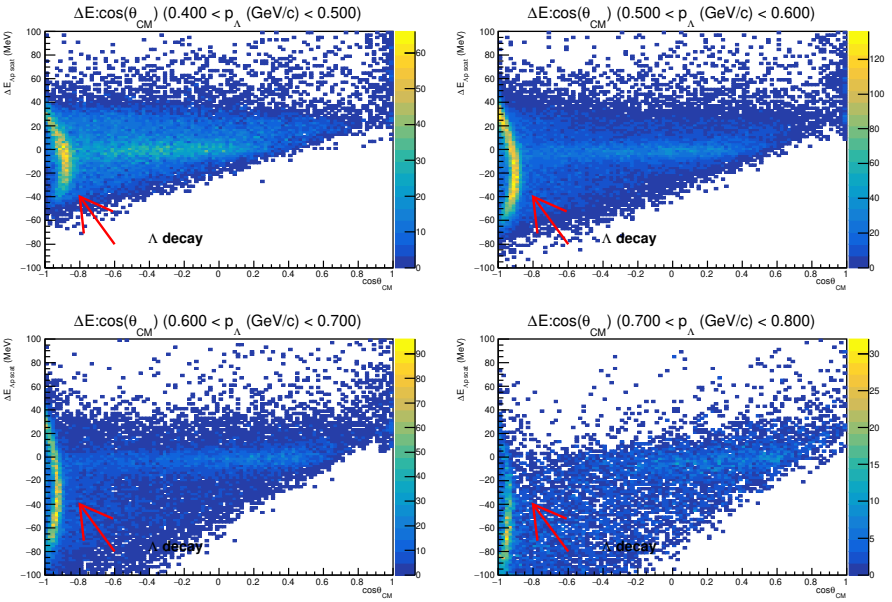

Figure 5.5: Correlation between the scattering angle and ΔE for the recoil proton analysis. The protons from Λ decay make a locus around backward angle region ($\cos\theta < -0.8$).

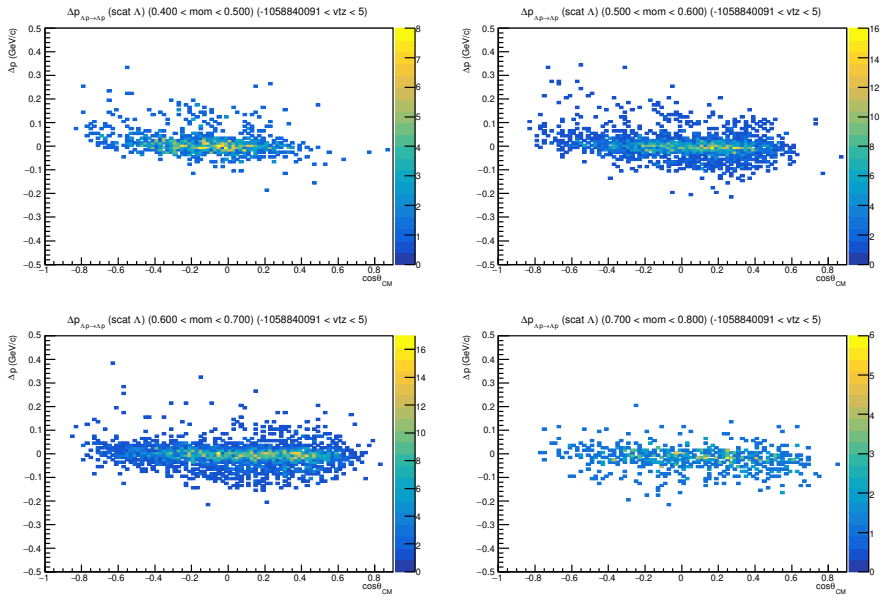

Figure 5.6: Correlation between the scattering angle ($\cos\theta$) and Δp for the scattered Λ analysis after applying the background rejection cuts. The Λ decay events at ($\cos\theta$, Δp) =(1, 0) are not shown. The locus at $\Delta p = 0$ corresponds to the Λp scattering.

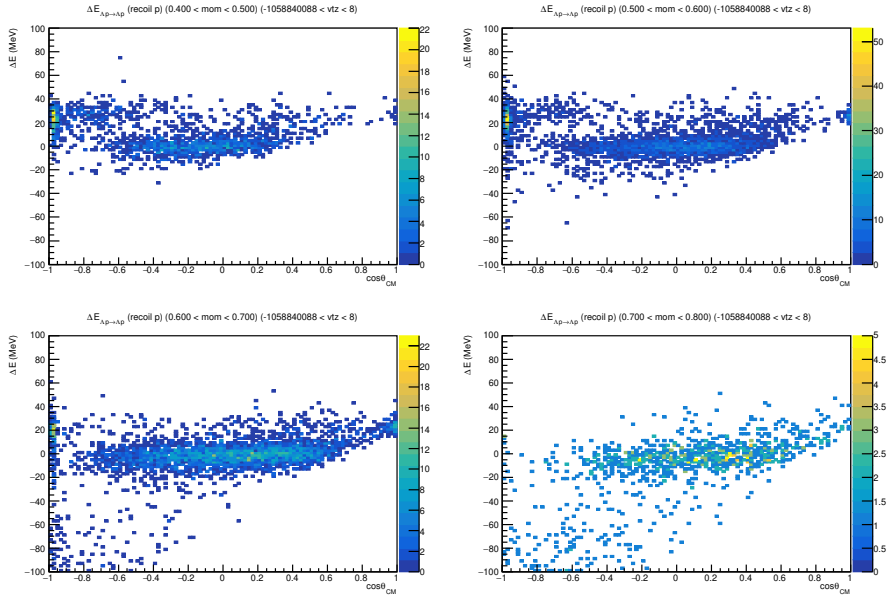

Figure 5.7: Correlation between the scattering angle and ΔE for the recoil proton analysis after applying the background rejection cuts. Λ decay background still remains backward angle region ($\cos\theta < -0.8$).

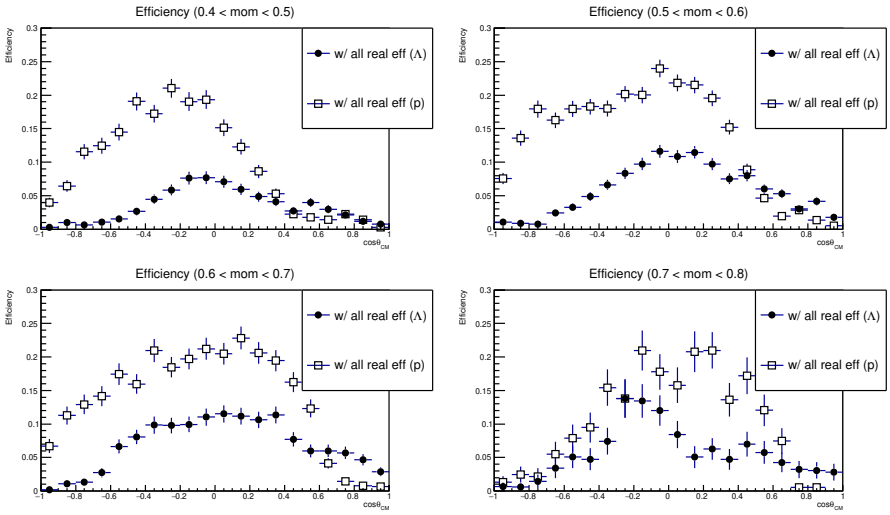

Figure 5.8: Scattering angle dependence of the detection efficiencies for the scattered Λ (closed circle) and the recoil proton (open box) for four momentum regions. The branching ratio of the $\Lambda \to \pi^- p$ mode is taken into account. In this estimation, two-proton cut is not applied to show the acceptance for proton and Λ separately.

total cross section of the Λp scattering is assumed to be 15, 10, 20 and 12 mb, respectively, based on the past experimental data and theoretical calculation. The angular dependence is simply assumed to be flat. Realistic energy resolution is used for the BGO calorimeter and CFT based on the E40 results. The contribution from background events are shown by the colored histogram. In the lower beam momentum region, the main background is pp scattering which were not removed by the rejection cut. However, the peak of Λp scattering can be clearly identified. This means that the background level is enough small.

5.4 Derivation of the differential cross sections of the Λp elastic scattering

The differential cross section is defined by this equation

$$\frac{d\sigma}{d\Omega} = \frac{\sum_{i_{vtz}} \frac{N_{scat}(i_{vtz},\cos\theta)}{\epsilon(i_{vtz},\cos\theta)}}{\rho \cdot N_{Avo} \cdot L \cdot d\Omega}, \tag{5.1}$$

where ρ, N_{Avo} and L represent the target density, Avogadoro's number and flight length of the Λ beam in the LH_2 target, respectively. The values of the numerator depends on the vertex position of the Λp scattering. i_{vtz} represents the index of the z vertex position from -150 mm to 150 mm with an interval of 30 mm. $N_{scat}(i_{vtz}, \cos\theta)$ and $\epsilon(i_{vtz,\cos\theta})$ represent the number of the Λp elastic scattering events and the detection efficiency of CATCH for scattering angle θ in the c.m. frame in the Λp scattering for z vertex position of i_{vtz}, respectively.

The total flight length L is estimated from the Monte Carlo simulation considering the Λ lifetime by using the obtained momentum and vertex information of Λ as inputs of this simulation. The number of the scattering events is estimated from the Δp and ΔE spectra

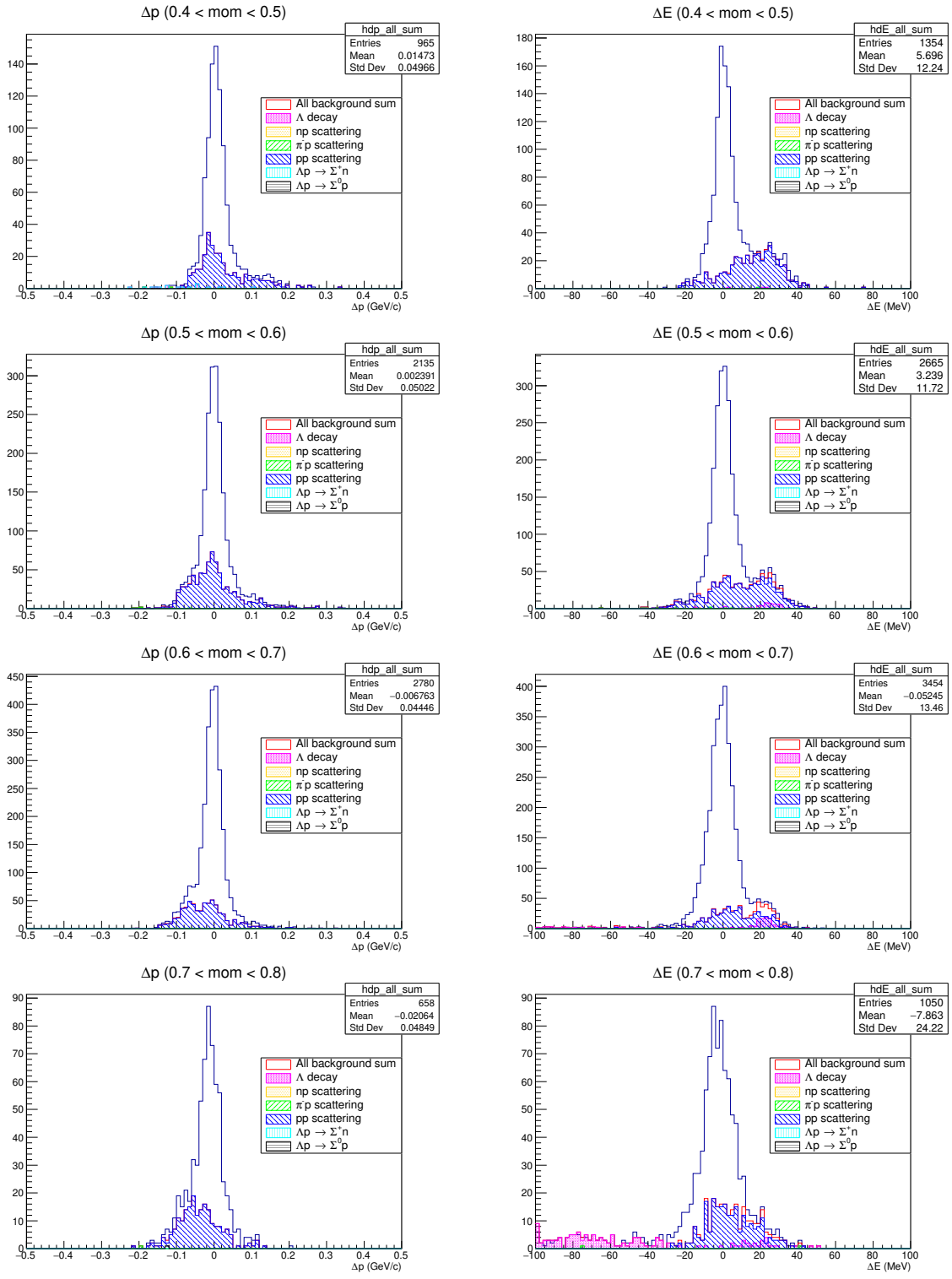

Figure 5.9: Projected Δp (left) and ΔE (right) spectra for angular regions of $\cos\theta < 0.9$ and $\cos\theta > -0.8$, respectively. Background are decomposed to understand each contribution. Above the ΣN threshold around 0.64 GeV/c, the contribution from inelastic channels ($\Lambda p \to \Sigma^+ n, \Lambda p \to \Sigma^0 p$) are also taken into account.

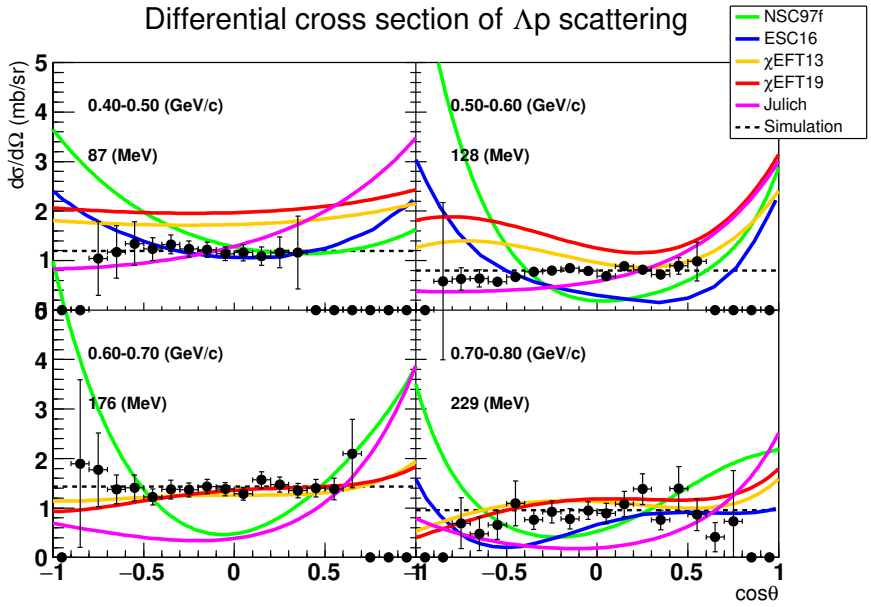

Figure 5.10: Simulated results for the differential cross section measurement of the Λp scattering in the momentum range from 0.4 to 0.8 GeV/c with 0.1 GeV/c momentum interval with 50M Λ beam. Theoretical calculations are also presented.

for the scattered Λ and recoil proton, respectively, for each scattering angle θ. For the efficiency, we make the efficiency table as shown in Figure 5.8. In the present analysis, the efficiency table with two-proton cut should be used.

In the present experiment, the Λ beam is expected to be highly polarized. In this case, the differential cross section for the unpolarized Λ beam is expressed as the mean of $(\frac{d\sigma}{d\Omega})_L$ and $(\frac{d\sigma}{d\Omega})_R$, which are differential cross sections for Λ scattered to left and right sides for the Λ spin axis, respectively. Detail of this analysis is described in next chapter. Figure 5.10 shows the expected differential cross section accuracy by calculating the mean of $(\frac{d\sigma}{d\Omega})_L$ and $(\frac{d\sigma}{d\Omega})_R$ for 50M Λ beam during about 30 days beam time. About 10% statistical accuracy is expected for scattering angle of $(\cos\theta = 0)$ from this beam time. For the D_y^y measurement, we request 100M Λ beam in total. Then, we can measure the differential cross section with tighter momentum step of 50 MeV/c as shown in Figure 5.11. At the Λ beam momentum around the ΣN threshold, the cross section is expected to change very much due to both the tensor force in the ΛN-ΣN coupling and the contribution from ALS. Therefore, momentum dependence of the differential cross section with 50 MeV/c step is very important measurement. By accumulating 100M Λ beam, we can achieve 10% level statistical accuracy with this momentum step.

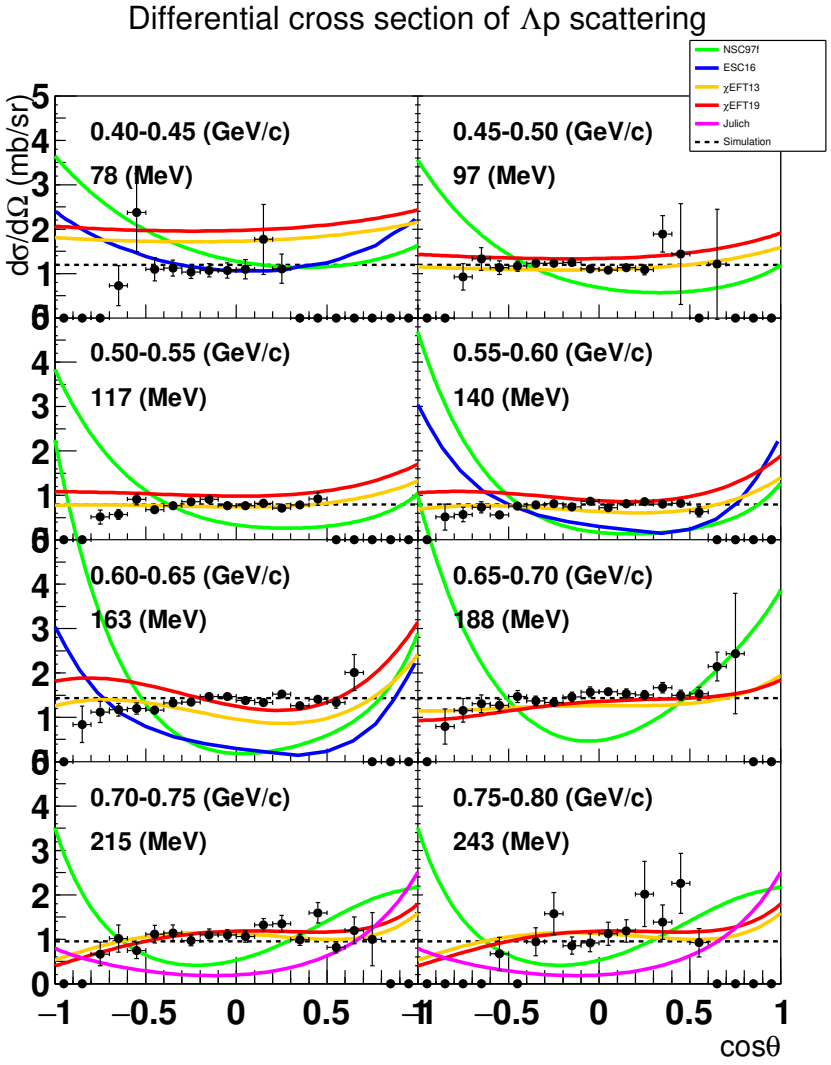

Figure 5.11: Simulated results for the differential cross section measurement of the Λp scattering in the momentum range from 0.4 to 0.8 GeV/c with 0.05 GeV/c momentum interval with 100M Λ beam. Theoretical calculations are also presented.

Chapter 6

Analysis of spin observables in the Λp scattering

In this chapter, we describe analysis of the polarization. At first, the polarization of the Λ beam is explained with the introduction of the quantization axis. Then the differential cross section for unpolarized beam and Analyzing power will be explained. Finally, polarization analysis for the scattered Λ is performed to derive the depolarization.

6.1 Λ beam polarization

One of the most important features of this experiment is to use the polarized Λ beam. In the $\pi^- p \to K^0\Lambda$ reaction around p_π =1.1 GeV/c, the high polarization is expected with respect to the (π^-, K^0) production plane. At first, we define the quantization axes for the Λ polarization as shown in Figure 6.1. The polarization axis of the Λ spin is the normal vector of the (π^-, K^0) plane. The axes are described as the following relations,

$$\boldsymbol{y} = \boldsymbol{p}_{\boldsymbol{\pi^-}} \times \boldsymbol{p}_{\boldsymbol{K^0}}, \tag{6.1}$$

$$\boldsymbol{z} = \boldsymbol{p}_{\boldsymbol{\Lambda}}, \tag{6.2}$$

$$\boldsymbol{x} = \boldsymbol{y} \times \boldsymbol{z}. \tag{6.3}$$

The y axis is represented by the outer product between incident π^- momentum vector and outgoing K^0 momentum vector. We define the z axis to be the Λ beam direction. Then the x axis is defined as the outer product between the y and z axes.

Figure 6.2 (left) shows the old measurement of the Λ polarization. Figure 6.2 (right) shows the experimental coverage for the K^0 angle in the c.m. system. In order to estimate the polarization of each Λ beam momentum, we overlaid the $\cos\theta$ distributions for each Λ momentum region. The Λ polarization becomes $\sim$100% for the angular region of $\cos\theta < 0.8$. Therefore 100% polarized Λ beam can be obtained for Λ beam with momentum larger than 0.5 GeV/c. Above 0.5 GeV/c, the polarization phenomena are expected to appear from the theoretical calculations. In the coordinate system at rest for Λ, the angular distribution of the emitted proton is represented by the following equation,

$$\frac{1}{N_0}\frac{dN}{d\cos\theta_p} = \frac{1}{2}(1 + \alpha P_\Lambda \cos\theta_p), \tag{6.4}$$

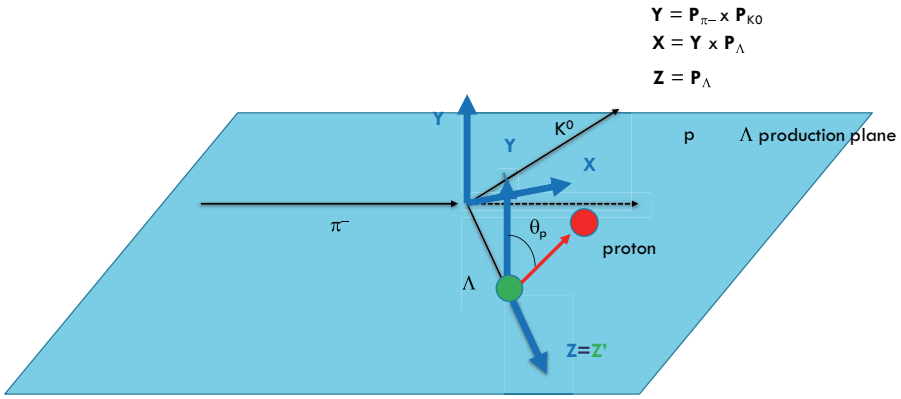

Figure 6.1: Definition of the quantization axes. The spin quantization axis is the y axis which is normal to the (π^-, K^0) production plane. The z axis is set to be the Λ beam direction and the x axis is defined as the outer product between the y and z axes.

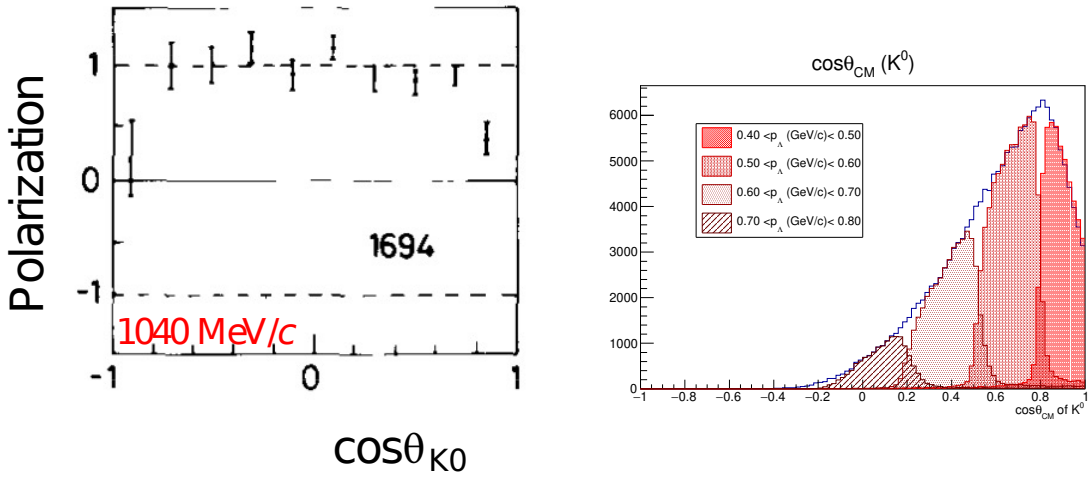

Figure 6.2: Left : Λ polarization in the $\pi^- p \to K^0\Lambda$ reaction measured by R.D. Baker *et al.* [47]. Right : Angular distribution of K^0 in the CM system accepted by the SKS spectrometer. The angular distribution for each Λ momentum is also shown.

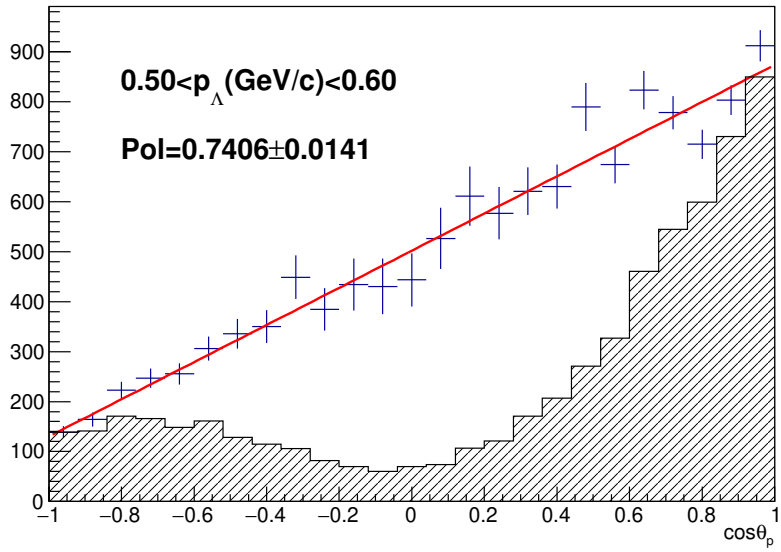

Figure 6.3: $\cos\theta_p$ distribution for the emitted proton measured by CATCH for the simulated events where the Λ polarization and asymmetry parameter are set to be 1.0 and 0.75, respectively. The data points with error bar represents the acceptance corrected angular distribution and are fitted by the expected angular distribution function in equation 6.4.

where P_Λ denotes the Λ polarization and α denotes asymmetry parameter. This asymmetry parameter has been measured with a good precision by BES3 collaboration [48] as

$$\alpha = 0.750 \pm 0.009 \pm 0.004. \tag{6.5}$$

For the polarization measurement, we will use this α value. θ_p is the angle of the proton direction from the polarization axis in the coordinate system at rest for Λ.

We explain how to measure the Λ beam polarization. The angular distribution of proton can be measured by CATCH. Hatched histogram in Figure 6.3 shows the $\cos\theta_p$ distribution measured by CATCH for the simulated events where the Λ polarization and asymmetry parameter are set to be 1.0 and 0.75, respectively. Due to the detector acceptance, the detected event around $\cos\theta_p = 0$ are suppressed. In order to reproduce the original angular distribution, this angular distribution should be corrected with the detector acceptance. The acceptance can be estimated from the angular dependence of the detection ratio for the unpolarized Λ in the simulation. Then corrected distribution shown as the plot with error bar in Figure 6.3 can be obtained by applying the acceptance correction to the hatched histogram. This corrected distribution is fitted with the function of equation 6.4 and the product of polarization and asymmetry parameter can be obtained from the slope parameter. The assumed αP_Λ value of 0.75 could be reconstructed from about 80k Λ events in the simulation. In the experiment, huge numbers of Λ are used to determine the polarization value and the statistical error is negligibly small. For the estimation of Analyzing power and depolarization in the following sections, we neglect the error of the Λ beam polarization.

6.2 Measurement of Analyzing power A_y

Analyzing power A_y can be derived by measuring the left-right asymmetry of the scattering for the Λ spin axis. In general, the differential cross section for polarized beam is represented as

$$\Big(\frac{d\sigma}{d\Omega}\Big)= \Big(\frac{d\sigma}{d\Omega}\Big)_0(1 + A_y(\theta)P_\Lambda \cos\phi), \tag{6.6}$$

where $\Big(\frac{d\sigma}{d\Omega}\Big)_0$ denotes the differential cross section for unpolarized beam, P_Λ denotes the Λ beam polarization and ϕ denotes the azimuthal angle. The azimuthal angle ϕ is defined as the crossing angle between the normal vectors for the Λ production plane and Λp scattering plane as shown in Figure 6.10 in next section.

Here, we define differential cross sections obtained for the left scatted Λ (x direction) and right scattered Λ ($-x$ direction) separately . $\Big(\frac{d\sigma}{d\Omega}\Big)_L$ represents the differential cross section obtained from the left scattered Λ. On the other hand, $\Big(\frac{d\sigma}{d\Omega}\Big)_R$ represents the differential cross section obtained from the right scattered Λ. These left and right differential cross sections are represented by the following expressions.

$$\begin{aligned}\Big(\frac{d\sigma}{d\Omega}\Big)_L &= \frac{1}{\pi}\Big(\frac{d\sigma}{d\Omega}\Big)_0 \int_{-\pi/2}^{\pi/2}(1 + A_y(\theta)P_\Lambda \cos\phi)d\phi &(6.7)\\ &= \Big(\frac{d\sigma}{d\Omega}\Big)_0(1 + \frac{2P_\Lambda}{\pi}A_y(\theta)) &(6.8)\end{aligned}$$

$$\begin{aligned}\Big(\frac{d\sigma}{d\Omega}\Big)_R &= \frac{1}{\pi}\Big(\frac{d\sigma}{d\Omega}\Big)_0 \int_{\pi/2}^{3\pi/2}(1 + A_y(\theta)P_\Lambda \cos\phi)d\phi &(6.9)\\ &= \Big(\frac{d\sigma}{d\Omega}\Big)_0(1 - \frac{2P_\Lambda}{\pi}A_y(\theta)) &(6.10)\end{aligned}$$

Then Analyzing power and the differential cross section for unpolarized beam can be obtained as follows,

$$\Big(\frac{d\sigma}{d\Omega}\Big)_0 = \frac{1}{2}\Big(\Big(\frac{d\sigma}{d\Omega}\Big)_L + \Big(\frac{d\sigma}{d\Omega}\Big)_R\Big) \tag{6.11}$$

$$A_y(\theta) = \frac{\pi}{2P_\Lambda}\frac{\Big(\frac{d\sigma}{d\Omega}\Big)_L - \Big(\frac{d\sigma}{d\Omega}\Big)_R}{\Big(\frac{d\sigma}{d\Omega}\Big)_L + \Big(\frac{d\sigma}{d\Omega}\Big)_R} \tag{6.12}$$

In practice, $\Big(\frac{d\sigma}{d\Omega}\Big)_L$ is derived from scattered Λ to the left side or recoil proton to the right side. $\Big(\frac{d\sigma}{d\Omega}\Big)_R$ is derived from scattered Λ to the right side or recoil proton to the left side. Figure 6.4 shows the efficiencies to detect proton and Λ for left and right sides, separately.

We estimated the accuracy for the Analyzing power A_y assuming $A_y = 0$, that is, no left-right asymmetry in the Λp scattering. Figure 6.5 (left) and (right) show $\Big(\frac{d\sigma}{d\Omega}\Big)_L$ derived from the scattered Λ to the left side and the recoil proton to the right side, respectively.

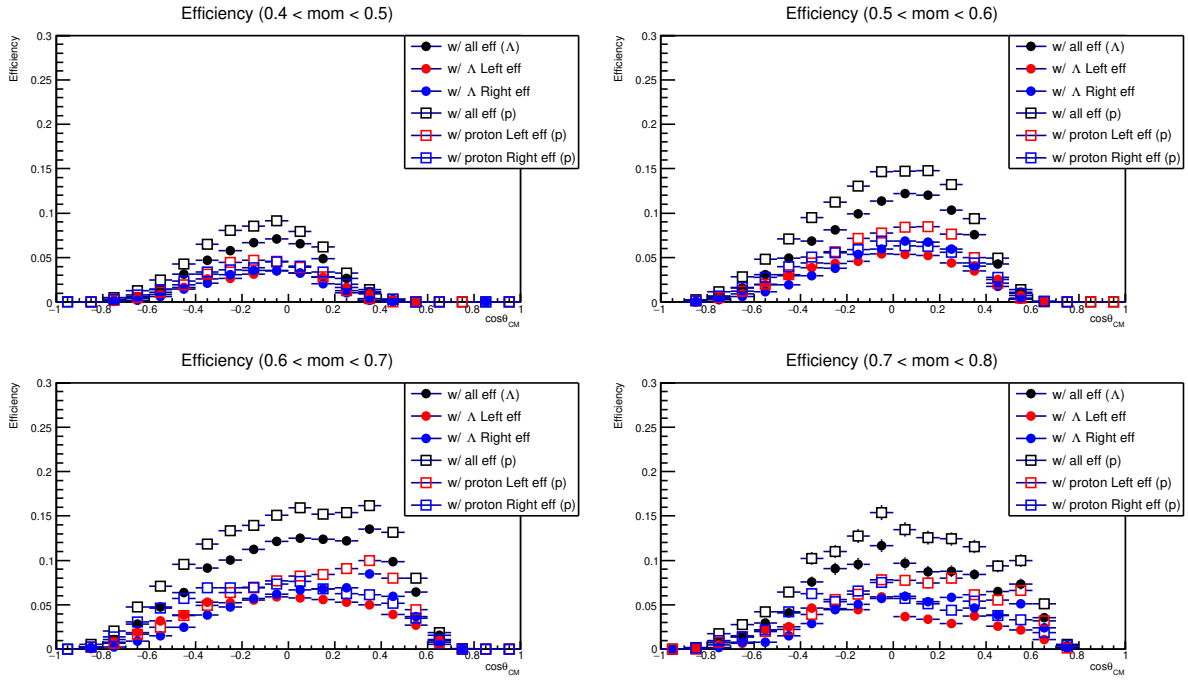

Figure 6.4: Scattering angle dependence of the detection efficiencies for the scattered Λ and recoil proton. Efficiencies for left side case and right side case are represented as blue and red points, respectively, for both Λ and proton.

These two histograms show the same observables and are identical within error. Finally $\left(\frac{d\sigma}{d\Omega}\right)_L$ is obtained as the weighted mean of these two measurements from Λ and proton. $\left(\frac{d\sigma}{d\Omega}\right)_R$ is also derived with the same procedure. Figure 6.6 (left) and (right) show $\left(\frac{d\sigma}{d\Omega}\right)_R$ derived from the the scattered Λ to the right side and $\left(\frac{d\sigma}{d\Omega}\right)_R$ derived from the recoil proton to the left side, respectively. Then the weighted mean of these values are calculated as the final value for $\left(\frac{d\sigma}{d\Omega}\right)_R$. In Figure 6.7, $\left(\frac{d\sigma}{d\Omega}\right)_L$ and $\left(\frac{d\sigma}{d\Omega}\right)_R$ are shown. Finally, A_y can be obtained based on equation 6.12 from $\left(\frac{d\sigma}{d\Omega}\right)_L$ and $\left(\frac{d\sigma}{d\Omega}\right)_R$. Figure 6.8 shows the expected A_y measurement for 50M Λ beam. In the higher momentum range, the error becomes large due to the limited statistics of the detected Λp scattering event. However, in the momentum range from 0.4 to 0.7 GeV/c, typically 10% of statistical error is estimated for the angular region of $\cos\theta = 0$. For the spin observable measurement, the angular step is modified to $d\cos\theta = 0.2$ to improve the statistical error. Especially in the Λ momentum region around the ΣN threshold (630 MeV/c), the theoretical predictions of A_y are very different with each other. The precise determination of both differential cross section and A_y is essential to improve these theoretical models. Figure 6.9 shows the expected result for 100M Λ beam. The errors can be reduced by a factor of 0.8.

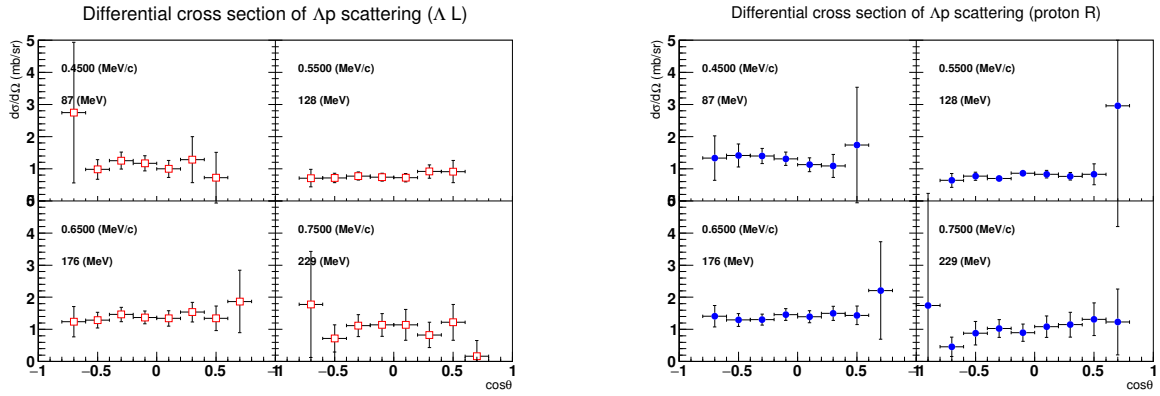

Figure 6.5: $\left(\frac{d\sigma}{d\Omega}\right)_L$ derived from Λ scattered to the left side (left figure) and from recoil proton scattered to the right side (right figure).

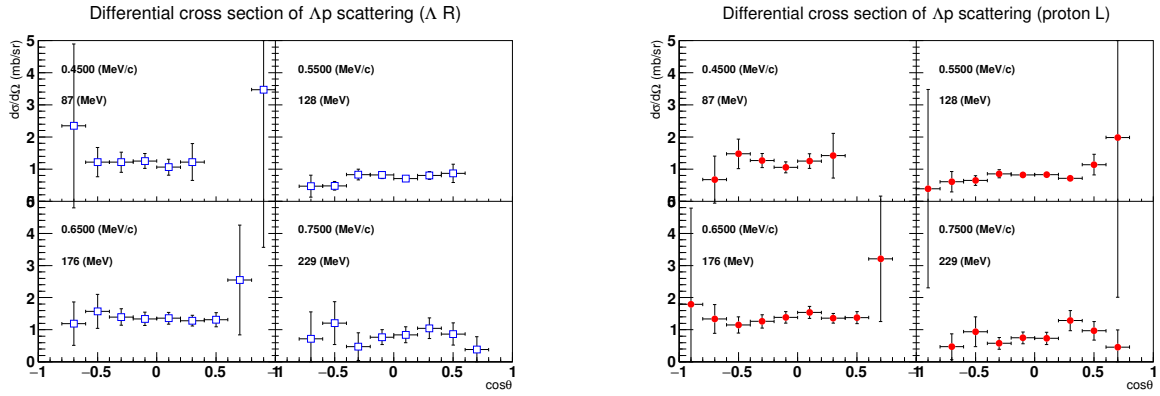

Figure 6.6: $\left(\frac{d\sigma}{d\Omega}\right)_R$ derived from Λ scattered to the right side (left figure) and from recoil proton scattered to the left side (right figure).

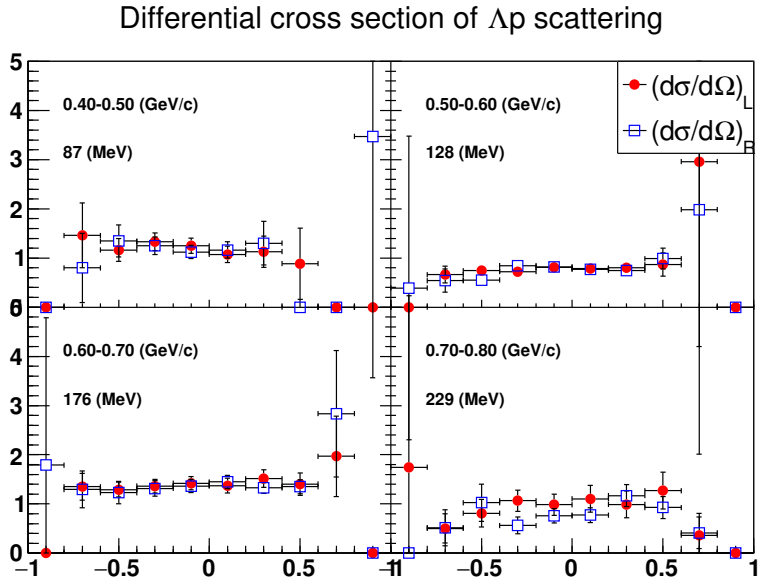

Figure 6.7: Differential cross sections of $\left(\frac{d\sigma}{d\Omega}\right)_L$ and $\left(\frac{d\sigma}{d\Omega}\right)_R$. These differential cross sections are obtained as the weighted mean of each differential cross section derived from Λ and proton.

6.3 Measurement of Depolarization D_y^y

Depolarization in the Λp scattering can be obtained by measuring the polarizations of Λ before and after the scattering with respect to the Λp scattering plane. The Λp scattering plane is defined as a plane including the Λ beam and the scattered Λ as shown in Figure 6.10. The Λ polarization axis is the normal vector of this Λp scattering plane. Axes for this Λp scattering are defined as the following relations,

$$\boldsymbol{z'} = \boldsymbol{z} = \boldsymbol{p_\Lambda}, \tag{6.13}$$
$$\boldsymbol{y'} = \boldsymbol{z'} \times \boldsymbol{p_{\Lambda scat}}, \tag{6.14}$$
$$\boldsymbol{x'} = \boldsymbol{y'} \times \boldsymbol{z'}, \tag{6.15}$$

where the z' and y' axes correspond to the Λ beam direction and the Λ polarization axis, respectively. Opening angle between the y and y' axes is the azimuthal angle ϕ of the Λp scattering. The polarization of the Λ beam can be described as $P_\Lambda \cos\phi$ with respect to the Λp scattering plane with an azimuthal angle ϕ.

The polarization of the scattered Λ is derived from the up-down asymmetry of the decay proton from Λ for the Λp scattering plane. Due to the limitation of the event number, the polarization is obtained simply from the following equation

$$P_{scat} = \frac{2}{\alpha}\frac{N_U - N_D}{N_U + N_D}, \tag{6.16}$$

where N_U and N_D represent the numbers of decay protons emitted to up and down sides for the Λp scattering plane, respectively, and α is the asymmetry parameter. The polarization of the scattered Λ can be represented by the following equation,

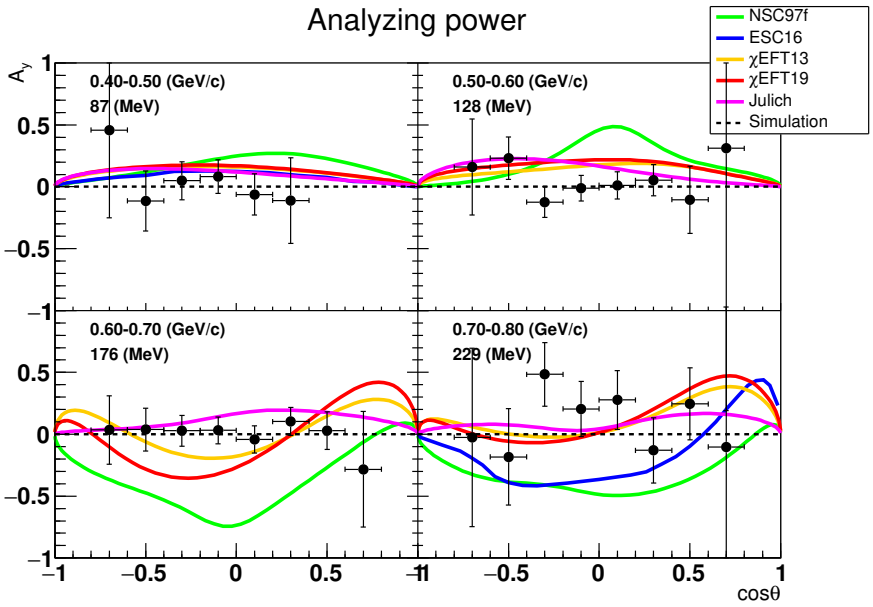

Figure 6.8: Expected A_y accuracy for 50M Λ beam. In the simulation, $A_y = 0$ is assumed as shown by the dotted lines. Theoretical calculations are also overlaid.

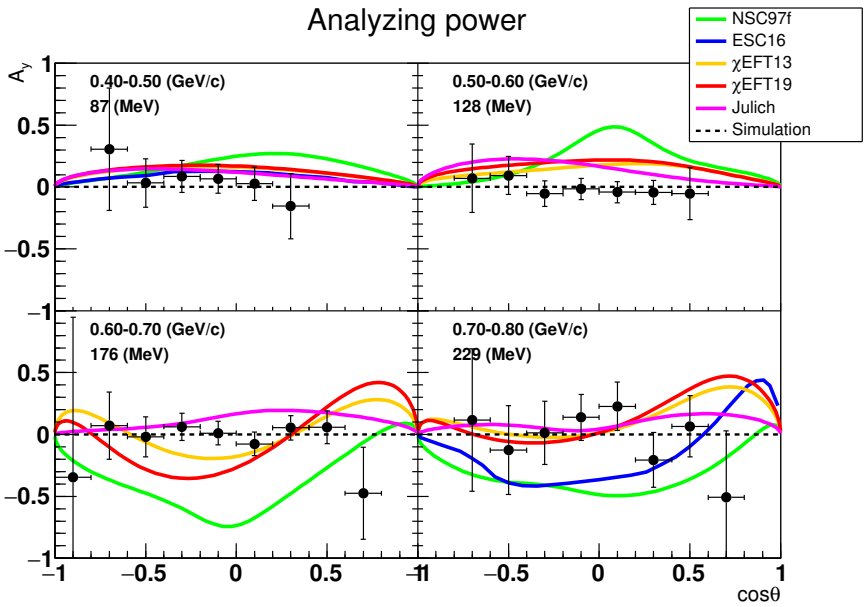

Figure 6.9: Expected A_y accuracy for 100M Λ beam. In the simulation, $A_y = 0$ is assumed as shown by the dotted lines. Theoretical calculations are also overlaid.

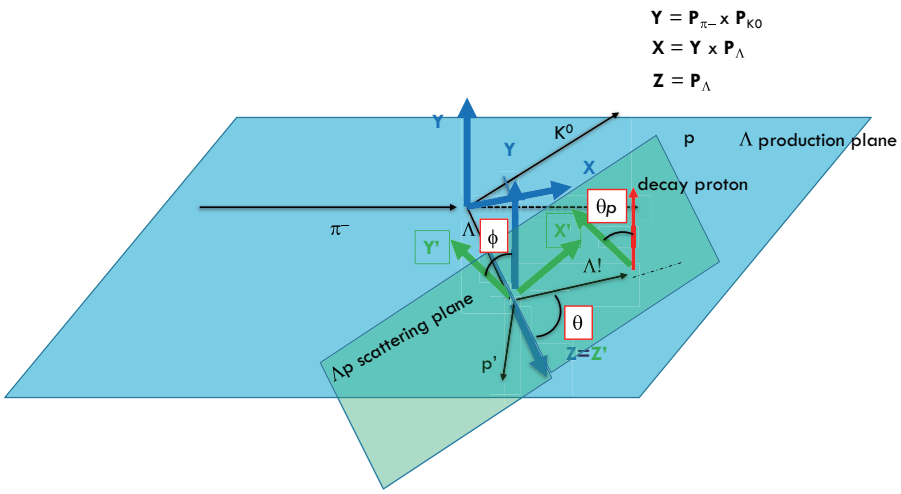

Figure 6.10: Definition of the quantization axes for the Λp scattering together with that for the Λ production plane. The spin quantization axis for the scattered Λ is the y' axis which is normal to the Λp scattering plane. The z' axis is set to be the Λ beam direction ($z' = z$) and the x' axis is defined as the outer product between the y' and z' axes.

$$P_{scat} = \frac{P + D_y^y P_\Lambda \cos\phi}{1 + P P_\Lambda \cos\phi}, \tag{6.17}$$

with depolarization (D_y^y), induced polarization of scattered Λ by the unpolarized Λ beam (P) and polarization of the Λ beam in the scattering plane ($P_\Lambda \cos\phi$). The induced polarization (P) is identical to the analyzing power (A_y) obtained with a polarized Λ beam.

A symmetric detector acceptance for the up and down directions is important for this measurement. In order to confirm how much the up-down symmetry is obtained, the up-down asymmetry $\frac{N_U - N_D}{N_U + N_D}$ for the unpolarized Λ beam was checked in the simulation. Figure 6.11 shows the ϕ dependence of the up-down asymmetry $\frac{N_U - N_D}{N_U + N_D}$ in this unpolarized case for several scattering angle θ. The red lines show the expected angular dependences. Although there exist some asymmetries in the detector acceptance depending on the azimuthal angle ϕ, almost symmetric result (value=0) is obtained. In the following depolarization analysis, the ϕ angular regions with a reasonable detector symmetry ($|\frac{N_U - N_D}{N_U + N_D}| < 0.15$) are used. When the Λ beam is polarized, the up-down asymmetry $\frac{N_U - N_D}{N_U + N_D}$ shows clear ϕ dependence as shown in Figure 6.12. In this simulation, no spin transfer ($D_y^y = 0$) and no induced polarization ($P = 0$) in the Λp scattering are assumed for simplicity. The beam polarization of $P_\Lambda = 1$ is also assumed based on the past measurement. The red liens show the expected ϕ dependences,

$$\frac{N_U - N_D}{N_U + N_D} = \frac{\alpha}{2} \cos\phi. \tag{6.18}$$

The simulated results show the similar ϕ dependence. Although this up-down asymmetry is still naive estimation of the polarization of the scattered Λ, the polarization can be estimated from this up-dwon asymmetry by using equation 6.16. Then, the depolarization (D_y^y) is also obtained from equation 6.17. In this D_y^y analysis, we have to check not only scattering angle θ dependence but also the azimuthal angle ϕ dependence. Therefore, 100M Λ beam is necessary to obtain a 10% level of accuracy at $\cos\theta = 0$ for the momentum region from 0.5

to 0.7 GeV/c. Figure 6.13 shows the expected result for the D_y^y measurement for 100M Λ beam. Due to the limitation of the statistics, errors in the high momentum region (0.7-0.8 GeV/c) are still large. However, in the middle momentum region (0.5 to 0.7 GeV/c) model difference between the chiral EFT and Nijmegen models can be clearly separated.

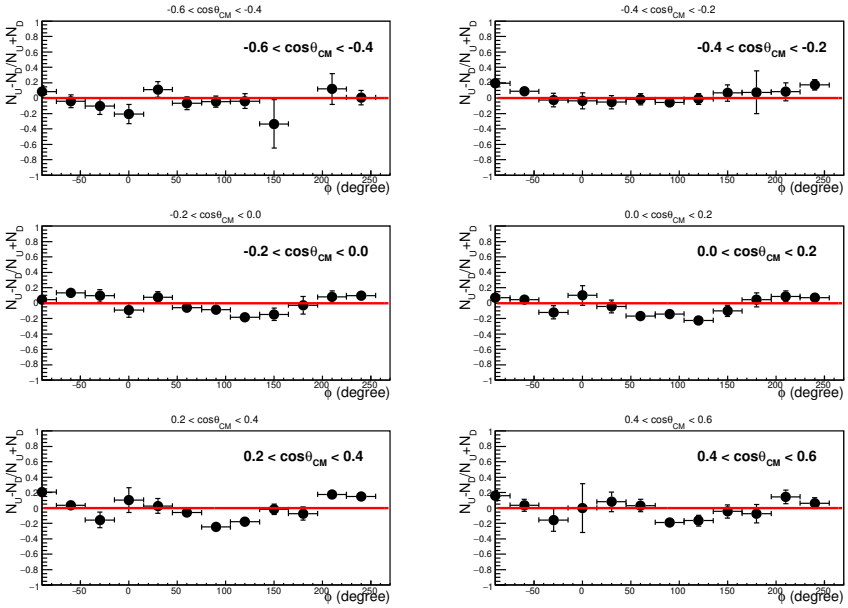

Figure 6.11: Up and down asymmetry of the decay proton with respect to the Λp scattering plane for the unpolarized Λ beam. The horizontal axis shows the azimuthal angle ϕ. The scattering angular dependence is also shown. In this case, no up-down asymmetry as shown by red lines are expected. Although there exist some asymmetries in the detector acceptance depending on the azimuthal angle ϕ, almost symmetric result (value=0) is obtained.

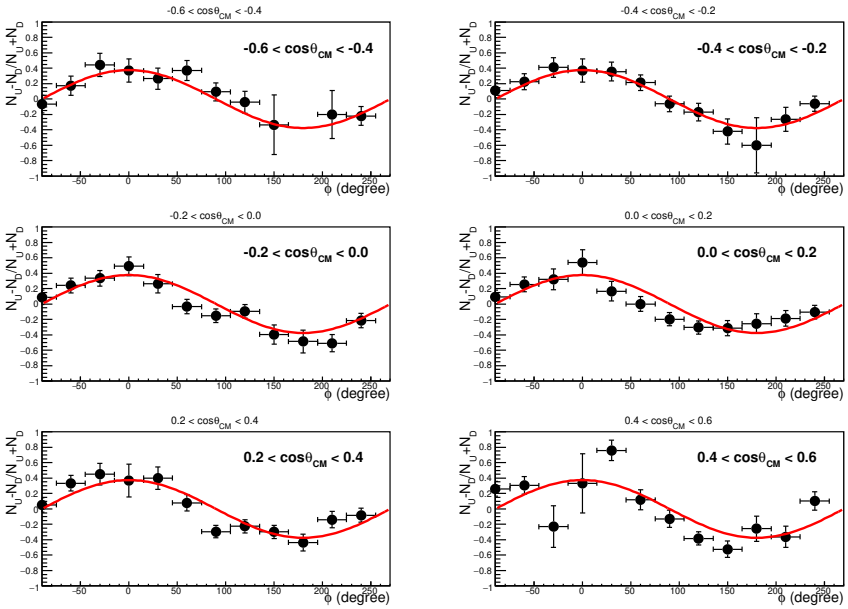

Figure 6.12: Up and down asymmetry of the decay proton with respect to the Λp scattering plane for the polarized Λ beam. In this case, up-down asymmetry is expected to be $\frac{\alpha}{2}\cos\phi$ as shown by red lines.

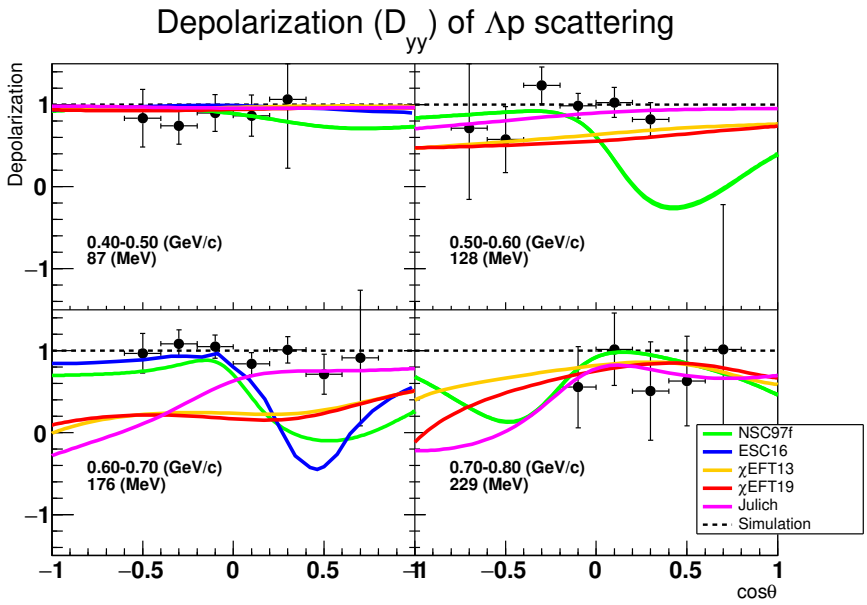

Figure 6.13: Expected D_y^y accuracy for 100M Λ beam. In this simulation, no spin transfer ($D_y^y = 0$) and no induced polarization ($P = 0$) in the Λp scattering are assumed for simplicity. The beam polarization of $P_\Lambda = 1$ is also assumed based on the past measurement. Theoretical calculations are also shown together. Due to the limitation of the statistics, errors in the high momentum region (0.7-0.8 GeV/c) are still large. However, in the middle momentum region (0.5 to 0.7 GeV/c) model difference between the chiral EFT and Nijmegen models can be clearly separated.

Chapter 7

Time schedule, cost and man power

Figure 7.1 shows the time schedule of development of detectors. As shown in this figure, many parts of detectors are already existing. As for the SKS spectrometer, we are going to utilize the present detector systems which were used in the K1.8 beam line. We need some repair works especially for large drift chambers (SDC3,4) at the downstream of the SKS magnet. Now we have already been doing the R&D work for developing the beam line hodoscopes and BFT-D detectors. We are developing a fine-segmented scintillator of $5\times5\times100$ mm^3 with a MPPC-array readout and time resolution of 80 ps has been obtained. The actual BH1 and BH2 detectors will be produced by FY2022. The design of BFT-D is also ongoing. BFT-D has 6 layers of a $xx'uu'vv'$ layer configuration with a 0.75 mm ϕ scintillation fibers. In this fiscal year, we will produce a prototype detector of a xx' layer configuration and check its performance. Finally, BFT-D will consists of two detector sets and these will be produced by FY2022. These detector development can be covered by KAKENSHI Grant (Kiban Kenkyu A). For SFT development, the experience in BFT development can be used. We need additional grant to produce this detector.

As for CATCH, even in the present configuration, this experiment can be performed. However, there might be some intervals until performing the experiment. Therefore, we are considering the upgrade of detector system. One of the biggest limitations in the present setup is that energies of π^- can not be measured due to the insufficient thickness of the BGO calorimeter. Even for protons with higher momentum more than 0.6 GeV/c, the present thickness is not enough to stop such high momentum protons. Although we have to optimize the detector configuration from now, in the forward region, where high momentum protons are emitted, additional BGO calorimeter will be placed to measure high energy protons. For the side region, where the proton energy is moderate, protons can be stopped in the present BGO detector. On the other hand, π^- from Λ decay and K^0_S decay can not be stopped. In order to measure the energy of such π^-, we are considering that the PiID counter around the BGO calorimeter is upgraded to range counter. In the present analysis method, we need some kinematical assumptions to reconstruct K^0_S and Λ. With this set up, these particles can be identified from the invariant mass spectrum. Especially, the K^0_S identification from the invariant mass is quite important to improve the Λ beam identification from the missing mass in the $\pi^- p \to K^0\Lambda$ reaction. In the present analysis for Λp scattering, we request two protons to suppress the background contamination from multi-π production. If the Λ beam identification is improved, we can request a looser cut to select to two charged particles (pair of proton and π^- or two protons) for the Λp scattering identification. This analysis can not only increase the yield of Λp scattering but also broaden

the angular coverage of the scattering. These simulation studies will be performed soon. We have also started R&D to develop a new ASIC for MPPC readout with a collaboration of KEK E-sys group as a framework of Open-It project. In this project, development of domestic ASIC which can satisfy multi purpose of MPPC readout is a motivation. Charge information from MPPC will be able to measured from waveform data. This is the very important point for CFT, which measures energy deposit in fibers. It might take longer time because it just has started. However, this is a very important development for all MPPC users.

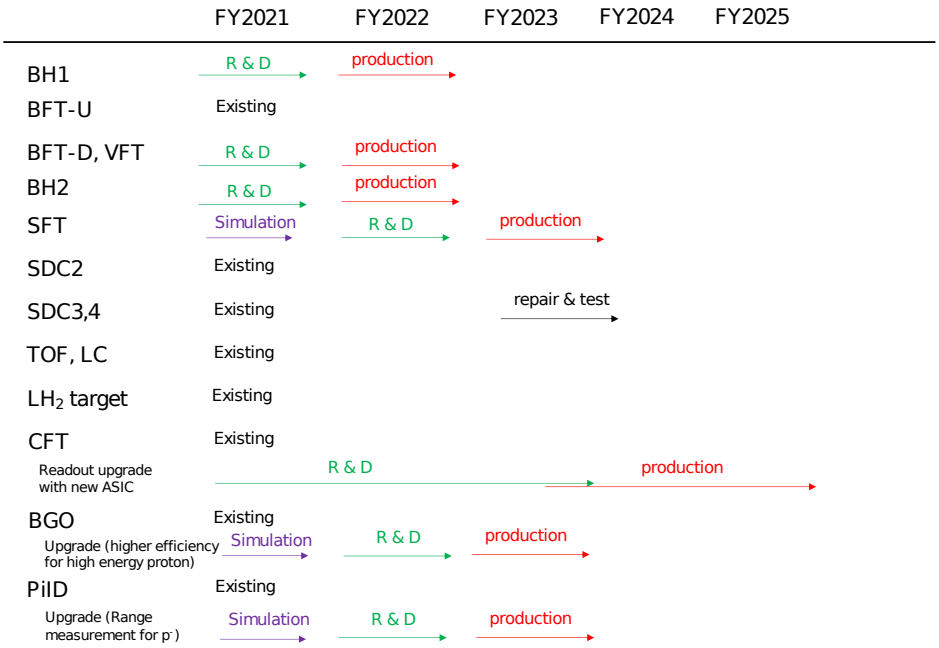

Figure 7.1: Time schedule of detector development.

Table 7.1: A list of items to be newly developed and its cost estimate.

Item	Cost [kJY]	Budget source
BH1, 2 (Scintillator & MPPC)	2,000	Kiban A
BH1,2 (HR-TDC)	1,000	Kiban A
BH1,2 (ADC)	under consideration	Additional grant is necessary
BFT-D (Detector)	4,000	Kiban A
BFT-D (MPPC)	1,500	Kiban A
BFT-D (Readout electronics)	under consideration	Additional grant is necessary
SFT (Detector)	4,000	Additional grant is necessary
SFT (MPPC)	1,500	Additional grant is necessary
SFT (Readout electronics)	under consideration	Additional grant is necessary
BGO crystal	10,000	Additional grant is necessary
BGO PMT.	3,000	Additional grant is necessary
BGO FADC	3,000	Additional grant is necessary
PiID range counter	3,000	Additional grant is necessary
PiID (MPPC)	1,000	Additional grant is necessary
PiID (Readout electronics)	under consideration	Additional grant is necessary
MPPC ASIC	under consideration	partially covered by Kiban A

Chapter 8

International situation and future prospect at J-PARC

Recently, femtoscopic measurements are widely applied to baryon pairs produced in pp and heavier ion collisions at LHC and RHIC [49, 50, 51, 52]. These measurements are very strong method to deduce the scattering length and effective range of the BB interactions including multi-strangeness systems. Because the femtoscopy is applied for the baryon pairs with small relative momentum, the S-wave information will be updated from these studies. In the proposed setup at J-PARC, measurement of the low energy YN scattering is rather difficult due to the difficulty in detection of low energy protons. However, in the present experiment, we can measure the differential information for higher momentum region. Therefore, these experiments are complemental relation. It should also be stressed that the differential information is quite awaited from theoretical side.

CLAS collaboration also has a potential to measure YN scattering from the re-scattering of hyperons produced by the photo-induced reaction [53]. In their analysis, the Λ momentum region is higher than 1 GeV/c. Therefore, relation between CLAS and this experiment is also complemental.

In J-PARC, Honda *et al.* [54] are considering a Λp scattering experiment at the High-p beam line in the secondary-particle mode. In the experiment at the High-p beam line, a wide momentum range ($0.4 < p(\mathrm{GeV}/c) < 2.0$) of Λ particle can be identified as Λ beam thanks to a large acceptance of the forward spectrometer and higher incident π^- beam momentum. This experiment is also important to measure the energy dependence of the ΛN cross section up to high momentum range (2 GeV/c), because the cross section at high energy is related to the short range interaction which becomes important at high density environment like the inner region of neutron star. Although there is an overlap in the Λ beam momentum region with the present experiment, there are unique features in both experiments.

- K1.1 : spin observable measurement around ΣN threshold region is a unique feature at the K1.1 beam line
- High-p : wide Λ momentum range up to 2 GeV/c and high statistics are unique feature at the High-p beam line

Therefore, both experiments can contribute the understanding of the YN two-body interaction.

In the proposed experiment at the K1.1 beam line, by accumulating several scattering observables, the data points ($d\sigma/d\Omega$, A_y and D_y^y) become comparable with the number of

phase shift values up to F or G waves. There is a possibility to derive the phase shift value from the global fit of all scattering observables like the NN case. In future, we should also consider this possibility for the construction of the realistic BB interaction model.

Bibliography

[1] R. Machleidt, Phys. Rev. C **63**, 024001 (2001).

[2] V. Stoks, R. Klomp, C. Terheggen, and J. de Swart, Phys. Rev. C **49**, 2950 (1994).

[3] R. Wiringa, V. Stoks, and R. Schiavilla, Phys. Rev. C **51**, 38 (1995).

[4] M. Oka, K. Shimizu, and K. Yazaki, Nucl. Phys. A **464**, 700 (1987).

[5] Y. Fujiwara, Y. Suzuki, and C. Nakamoto, Prog. Part. Nucl. Phys. **58**, 439 (2007).

[6] S. Aoki *et al.*, Prog. Theor. Exp. Phys. , 01A105 (2012).

[7] T. Inoue *et al.*, Nucl. Phys. A **881**, 28 (2012).

[8] H. Nemura *et al.*, EPJ Web of Conf. **175**, 05030 (2018).

[9] T. A. Rijken, V. G. J. Stoks, and Y. Yamamoto, Phys. Rev. C **59**, 21 (1999).

[10] M. M. Nagels, T. A. Rijken, and Y. Yamamoto, Phys. Rev. C **99**, 044003 (2019).

[11] J. Haidenbauer and U.-G. Meißner, Phys. Rev. C **72**, 044005 (2005).

[12] B. Sechi-Zorn, B. Kehoe, J. Twitty, and R. A. Burnstein, Phys. Rev. **175**, 1735 (1968).

[13] G. Alexander *et al.*, Phys. Rev. **173**, 1452 (1968).

[14] J. A. Kadyk, G. Alexander, J. H. Chan, P. Gaposchkin, and G. H. Trilling, Nucl. Phys. B **27**, 13 (1971).

[15] J. M. Hauptman, J. A. Kadyk, and G. H. Trilling, Nucl. Phys. B **125**, 29 (1977).

[16] R.Engelmann, H.Filthuth, V.Hepp, and E.Kluge, Phys. Lett. **21**, 587 (1966).

[17] F. Eisele, H. Filthuth, W. Fölisch, V. Hepp, and G. Zech, Phys. Lett. **37B**, 204 (1971).

[18] D. Stephen, Ph.D. thesis (1970).

[19] Y. Kondo *et al.*, Nucl. Phys. A **676**, 371 (2000).

[20] J. K. Ahn *et al.*, Nucl. Phys. A **761**, 41 (2005).

[21] O. Hashimoto and H. Tamura, Prog. Part. Nucl. Phys. **57**, 564 (2006).

[22] Y. Yamamoto, T. Motoba, and T. Rijken, Prog. Theor. Phys. Suppl. **185**, 72 (2010).

[23] P. Demorest *et al.*, Nature **467**, 1081 (2010).

[24] S. N. Nakamura *et al.*, Proposal to the 32nd J-PARC PAC **High precision spectroscopy of Λ hypernuclei with the (π^+, K^+) reaction**.

[25] K. Miwa *et al.*, J. Phys. : Conf. Ser. **1643**, 012174 (2020).

[26] K. Miwa *et al.*, arXiv:2104.13608 (2021).

[27] S. Ishikawa, M. Tanifuji, Y. Iseri, and Y. Yamamoto, Phys. Rev. C **69**, 034001 (2004).

[28] J. Haidenbauer, K. Holinde, V. Mull, and J. Speth, Phys. Lett. B **291**, 223 (1992).

[29] M. Kurosawa *et al.*, Jps. J. Appl. Phys. **45**, 4204 (2006).

[30] J. Haidenbauer, S. Petschauer, N. Kaiser, U.-G. Meißner, A. Nogga, and W. Weise, Nucl. Phys. A **915**, 24 (2013).

[31] J. Haidenbauer, U.-G. Meißner, and A. Nogga, Eur. Phys. J. A **56**, 91 (2020).

[32] J. Haidenbauer, Private communication ().

[33] J. Haidenbauer and U.-G. Meißner, arXiv:2105.00836 (2021).

[34] J. Haidenbauer, private communication ().

[35] T. A. Rijken, private communication .

[36] Y. Yamamoto, T. Furumoto, N. Yasutake, and T. A. Rijken, Phys. Rev. C **90**, 045805 (2014).

[37] M. Isaka, Y. Yamamoto, and T. A. Rijken, Phys. Rev. C **95**, 044308 (2017).

[38] S. Petschauer, N. Kaiser, J. Haidenbauer, U.-G. Meißner, and W. Weise, Phys. Rev. C **93**, 014001 (2016).

[39] S. Petschauer, J. Haidenbauer, N. Kaiser, U.-G. Meißner, and W. Weise, Nucl. Rev. A **957**, 347 (2017).

[40] M. Kohno, Phys. Rev. C **97**, 035206 (2018).

[41] J. Haidenbauer and I. V. na, Eur. Phys. J. A **56**, 55 (2020).

[42] T. Sakao *et al.*, JPS Conf. Proc. **33**, 011133 (2021).

[43] T. Takahashi *et al.*, PTEP **2012**, 02B010 (2012).

[44] J. J. Jones *et al.*, Phys. Rev. Lett. **26**, 860 (1971).

[45] T. M. Knasel *et al.*, Phys. Rev. D **11**, 1 (1975).

[46] T. O. Binford *et al.*, Phys. Rev. **183**, 1134 (1969).

[47] R. D. Baker *et al.*, Nucl. Phys. B **141**, 29 (1978).

[48] M. Ablikim *et al.*, Nature Physics **15**, 631 (2019).

[49] L. Adamczyk and others (STAR Collaboration), Phys. Rev. Lett. **114**, 022301 (2015).

[50] S. Acharya and others (ALICE Collaboration), Phys. Rev. C **99**, 024001 (2019).

[51] K. Morita, T. Furumoto, and A. Onishi, Phys. Rev. C **91**, 024916 (2015).

[52] A. Collaboration), Phys. Lett. B **805**, 135419 (2020).

[53] J. W. Price *et al.*, AIP Conf. Proc. **2130**, 020004 (2019).

[54] R. Honda *et al.*, Letter of Intent for J-PARC PAC **http://j-parc.jp/researcher/Hadron/en/pac_2007/pdf/LoI_2020-08.pdf** (2020).